3D stochastic bicontinuous microstructures: Generation, topology and elasticity

Celal Soyarslan [a, *], Swantje Bargmann [a], Marc Pradas [b], Jörg Weissmüller [c, d]

[a] *Chair of Solid Mechanics, School of Mechanical Engineering and Safety Engineering, University of Wuppertal, Germany*
[b] *School of Mathematics and Statistics, The Open University, Milton Keynes, MK7 6AA, United Kingdom*
[c] *Institute of Materials Physics and Technology, Hamburg University of Technology, Hamburg, Germany*
[d] *Institute of Materials Research, Materials Mechanics, Helmholtz-Zentrum Geesthacht, Geesthacht, Germany*

ABSTRACT

Motivated by recent experimental investigations of the mechanical behavior of nanoporous metal we explore an efficient and robust method for generating 3D representative volume elements (RVEs) with strikingly similar behavior. Our approach adopts Cahn's method of generating a Gaussian random field by taking a superposition of standing sinusoidal waves of fixed wavelength but random in direction and phase. In its theory part, our study describes closed-form expressions for how the solid volume fraction affects the binarization level, mean structure size, specific surface area, averages of mean and Gaussian curvature, and the scaled topological genus. Based on numerical studies we report on criteria for achieving representative realizations of the structure by proper choice of the number of waves and element size. We also show that periodic structures are readily created. We analyze the mechanical properties considering linear and infinitesimal elasticity and evaluate the residual anisotropy (which can be made small) and the effective values of the Young's modulus and Poisson's ratio. The numerical results are in excellent agreement with experimental findings for the variation of stiffness with solid fraction of nanoporous gold made by dealloying. We propose scaling relations that achieve naturally a perfect agreement with the numerical and experimental data. The scaling relation for the stiffness accounts for a percolation-to-cluster transition in the random field microstructure at a finite solid fraction. We propose that this transition is the origin of the previously reported anomalous compliance of nanoporous gold.

© 2018 Acta Materialia Inc. Published by Elsevier Ltd. This is an open access article under the CC BY-NC-ND license (http://creativecommons.org/licenses/by-nc-nd/4.0/).

1. Introduction

Stochastic bicontinuous microstructures, in which two contiguous phases interpenetrate, are characteristic for many materials formed by decomposition of a homogeneous parent phase. Examples are spinodally decomposed metal alloys [1,2], polymer blends [3,4] or microemulsions [5], foams that can be polymeric, metallic or food [6] and network solids such as nanoporous metals made by dealloying solid solutions [7,8]. The properties of such microstructures depend on geometric or topological characteristics including the specific surface area, the tortuosity of transport paths through one or both of the phases, the characteristic structure size, and measures for connectivity, such as e.g. genus per unit volume. Here, we describe how spinodal-like stochastic microstructures can

be generated by a convenient and fast numerical algorithm and we explore their geometric and mechanical properties.

Our study is motivated by recent research in the field of nanoporous metals made by dealloying. A substantial body of experiments explores specifically the mechanical behavior of nanoporous gold made in this way [9—18]. Nanoporous materials made by dealloying can be understood as networks of nanoscale struts or "ligaments", typically with solid volume fractions between 0.25 and 0.50 [7—9]. While their microstructure is stochastic, their mechanical behavior is typically discussed with reference to the Gibson-Ashby scaling relations [6] which have been supported - on the modeling side - by periodic structures. However, the mechanical properties of dealloying-made nanoporous solids are not well described by the Gibson-Ashby scaling relations, and specifically their Young's modulus can be more than an order of magnitude less than predicted [14,19]. While surface excess elasticity has been ruled out as an explanation [20,21], nonlinear elastic behavior of the bulk may contribute [22]. Yet, the decisive issue appears to be

network connectivity [13,14,23,24], which may systematically vary with ligament size and solid fraction.

Cahn [1] showed that the composition field in the early stages of spinodal decomposition could be approximated by the superposition of waves with random direction but same wavelength. In one of the first computer simulations of microstructure evolution in materials science, Cahn showed that binarizing this composition field indeed yielded the bicontinuous microstructure of spinodally decomposed mixtures [1]. In the present work, we explore a modern numerical implementation of Cahn's algorithm, which efficiently generates 3D stochastic bicontinuous microstructures. We present closed-form expressions for specific surface area and scaled connectivity as a function of the wavelength and solid fraction. Using finite element simulations, we document the elastic behavior and the requirements on the size of the volume element (VE)[1] for achieving representative behavior. The numerical part of our study specifically focuses on the comparison to nanoporous gold, from which the experimental validation of our model emerges. We point out that a percolation-to-cluster transition at finite density can be related to the anomalously low stiffness of experimental nanoporous gold. We bring to the reader's attention an alternative scaling law, suggested by Roberts and Garboczi [25], which accounts for the transition and remains accurate over a wide range of solid volume fraction. Since many numerical simulation approaches use periodic boundary conditions, we show how volume elements with translational periodicity can be generated. We also provide a comparison between the results for aperiodic and periodic microstructures considering the predicted effective elastic properties and demonstrate that they are in very good agreement.

2. Methods of 3D generation of nanoporous metal microstructures

The 3D geometry of the microstructure of nanoporous gold has been characterized in experiment by tomographic reconstruction. Approaches were based on transmission electron microscopy [26—29], X-ray nanotomography [30—32], focused-ion-beam (FIB) sectioning [23,24,33,34] and atom-probe tomography [35]. These approaches reveal a random network of ligaments which are interconnected in nodes. The surface is found dominated by convex and saddle-shaped patches [33], so that the average of the mean curvature is positive [26,33]. The connectivity density is less than in regular geometric networks such as the gyroid structure [23], and it varies little when the mean structure size is varied by annealing-induced coarsening [24,33]. Experimental 3D microstructures have been used as the basis for numerical simulation of the mechanical response of nanoporous gold [23,24,32]. Studies working with large volume elements, as better representatives for macroscopic material response, find strength and stiffness in qualitative agreement with experimental mechanical tests [23,24].

While experimental reconstructions are distinguished by their realistic geometry, they are also restricted to specific realizations within the family of possible structures with the same stochastic building principles. Furthermore, systematic experiments exploring variations of the microstructure of nanoporous gold with solid fraction remain yet to be reported. Numerical simulation approaches, and specifically atomistic approaches such as molecular dynamics, also often require models that are compatible with 3D translational periodicity. In each instance, the available experimental database for 3D structures is not yet sufficient for comprehensive numerical studies. This highlights the need for the computational generation of model structures.

Computational generation methods often use deterministic periodic unit cell-based idealizations. This may involve heuristic constructions or constructions of (analytical) level surfaces, e.g., triply periodic minimal surface-based unit cells. The Kelvin model [36] consisting of a regular packing of tetra(kai)decahedra, its variations by Waire and Phelan [37] and the model of Gibson and Ashby [6,38] are among the most widely used idealized unit cells for nanoporous metals. Agglomeration of the mass in junctions is considered making use of modified rectangular unit cells in Refs. [39,40]. Periodic diamond cubic unit cells were recently used for modeling nanoporous gold samples [21].

Constructions of triply periodic bicontinuous cubic microdomain morphologies, which are generated by making use of triply periodic continuous minimal surfaces [41,42], constitute another attractive direction. These level surfaces and the developed microstructures have the symmetries of a crystallographic group such as cubic, tetragonal, rhombohedral, and orthorhombic symmetries. Their smooth surfaces allow incorporation of theories accounting for surface curvature effects more realistically. For the use of triply periodic minimal surface based microstructures in modeling of nanoporous gold samples, see e.g. Refs. [23,43,44]. Gyroids as approximants to nanoporous metal foams were investgated in Ref. [45]. Moreover, microstructures made up of single and double gyroids were used in computation of the specific surface area of nanoporous materials in Ref. [46].

Although periodic unit cell idealizations prove efficient and simple, they fall short in reflecting certain key morphological, topological and mechanical characteristics of nanoporous metals. On the morphological part, the 3D reconstructions emphasize a random, as opposed to periodic, structure. So far, no evidence of anisotropy in the mechanical response has been reported for nanoporous gold and the reconstructions appear isotropic. On the contrary, the structures generated by making use of the aforementioned heuristic constructions or constructions of (analytical) level surfaces show cubic anisotropy with high polarity in terms of their directional dependence of Young's modulus.

It is possible to bridge this gap by considering stochastic disorder in cell structures, see, e.g., [47—49]. Voronoi or Laguerre tessellations constitute a more systematic method in forming stochastic cells [50—53]. A specific step in this direction was the introduction of disorder in the diamond-based network structure of Ref. [21], which indeed provided qualitatively improved agreement with experiments.

Computational generation of stochastic bicontinuous geometries of nanoporous metals are often created at considerable computational expense. With attention to modeling dealloying-made metal network structures, several studies have used the simulation of spinodal decomposition via phase-field [54—56] or kinetic lattice Monte Carlo approaches [19,57]. These approaches achieve a striking similarity to the experimental reconstructions of dealloying-made metal network structures.

A computationally more efficient method of modeling phase-separation dynamics, i.e., the phase-ordering dynamics of thermodynamically unstable phases, is the use of cell dynamical systems [58—60], e.g., coupled maps and cellular automata.

Making use of leveled Gaussian random fields, in which the interfaces between cells are defined by level cuts of random fields [61], in computational generation of stochastic bicontinuous geometries constitutes an even more efficient approach. Leveled-wave models for random morphologies, which were initially proposed for bicontinuous material morphologies formed due to phase-separation [1], have found attention in various applications [25,62—64].

---

[1] A volume element does not have to be adequate in size to cover sufficient microstructural features and, thus, encapsulate the effective properties, as an RVE does.
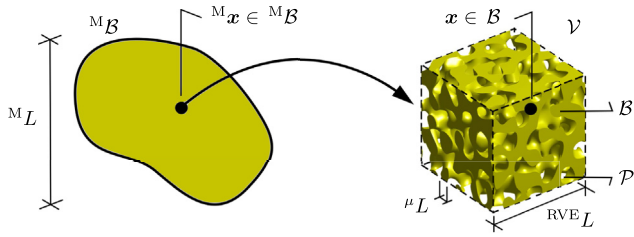
Fig. 1. The homogenized macrocontinuum is denoted by $^{M}\mathcal{B}$, and a typical point $^{M}\boldsymbol{x}\in{}^{M}\mathcal{B}$ encapsulates a microstructure $\mathcal{B}$ of volume $\mathcal{V}$. The associated length scales are denoted by ^{M}L and $^{\mu}L$ for the macroscopic structural scale and the characteristic size of a microstructural feature (e.g. ligament diameter), respectively. They satisfy the condition $^{M}L \gg {}^{RVE}L > {}^{\mu}L$, where ^{RVE}L represents the size of the representative volume, reflecting the mesoscale.

3. Gaussian random fields and microstructure generation

We start by introducing the notion of a continuum with microstructure and computational micro-to-macro transition [65,66] as sketched in Fig. 1.[2] Let $^{M}\mathcal{B}\subset\mathcal{R}^3$ denote the homogenized macrocontinuum. A typical point $^{M}\boldsymbol{x}\in{}^{M}\mathcal{B}$ has a representative volume $\mathcal{V}\subset\mathcal{R}^3$ that consists of two phases: the solid bulk phase, i.e. the metallic microstructure, and the pore phase, with their corresponding volumes denoted by $\mathcal{B}\subset\mathcal{R}^3$ and $\mathcal{P}\subset\mathcal{R}^3$, respectively. We then have $\mathcal{V} = \mathcal{B} + \mathcal{P}$, and the interface of the microstructure is denoted by $\partial\mathcal{B}$.

3.1. A specific random field

The microstructure considered here derives from the random field which is generated by superimposing standing sinusoidal waves of fixed wavelength and amplitude but random direction and phase [1]:

$$f(\boldsymbol{x}) = \sqrt{\frac{2}{N}}\sum_{i=1}^{N}\cos(\boldsymbol{q}_i\cdot\boldsymbol{x}+\varphi_i) \tag{1}$$

Here, $\boldsymbol{x}$ is the position vector, N represents the number of waves considered in the truncated series, and $\boldsymbol{q}_i$ and φ_i denote wave direction and wave phase of the ith wave, respectively. In our analysis, we fix the wave number to a constant value $q_i = |\boldsymbol{q}_i| = q_0$, with uniformly distributed wave directions over the solid angle 4π and wave phases uniformly distributed in the interval 0 to 2π. Under these conditions $f(\boldsymbol{x})$ is a Gaussian random field with $\langle f\rangle = 0$, $\langle f^2\rangle = 1$, and a two-point correlation function given as

$$C_2(r) = \langle f(\boldsymbol{x}_1)f(\boldsymbol{x}_2)\rangle = \frac{\sin(q_0 r)}{q_0 r}, \tag{2}$$

where brackets denote ensemble averages over realizations, and $r = |\boldsymbol{x}_1 - \boldsymbol{x}_2|$ (see Supplementary Material for the derivation details). If N is sufficiently large, the value of the random function $f(\boldsymbol{x})$ at a given position $\boldsymbol{x}$ follows a Gaussian distribution with $P(f) = e^{-f^2/2}/\sqrt{2\pi}$ and the mean wave direction $\boldsymbol{v} = \frac{1}{N}\sum_{i=1}^{N}\boldsymbol{n}_i$ approaches zero as a consequence of the central limit theorem. Then, f is an isotropic function, see Supplementary Material.

Given the random function (1), the different phases of the system are defined via a level cut ξ:

---

[2] Unless the microstructures show weak geometric disorder and/or weak mismatch in properties, the weak statement $^{RVE}L > {}^{\mu}L$ is replaced by the stronger [67] one $^{RVE}L \gg {}^{\mu}L$.

$$\begin{aligned}\boldsymbol{x}\in\mathcal{B} &\quad \text{if } f(\boldsymbol{x}) < \xi, \\ \boldsymbol{x}\in\partial\mathcal{B} &\quad \text{if } f(\boldsymbol{x}) = \xi, \\ \boldsymbol{x}\in\mathcal{P} &\quad \text{if } f(\boldsymbol{x}) > \xi.\end{aligned} \tag{3}$$

In this study, we create numerical realizations of the random field microstructure on regular 3D voxel lattices by summing up N waves (typically $N = 10000$) with randomly oriented $\boldsymbol{q}_i$ and random phases φ_i. We explore the variation of properties as the structure was repeatedly created with different initial settings of the random number generator; the individual structures in such studies are referred to as "realizations". Examples of microstructures for different values of ξ and for volume element size of 12 wavelengths are shown in Fig. 2.

3.2. Generating periodic structures

The microstructures generated using Eq. (1) along with Eq. (3) are generally not periodic. Periodicity can be accomplished by selecting a finite number of waves which have integer wave number in all directions and constant modulus. Our starting point is the field given by Eq. (1). We take $\boldsymbol{e}_1$, $\boldsymbol{e}_2$, $\boldsymbol{e}_3$ unit vectors of an orthonormal basis in real space and let all $\boldsymbol{q}_i$ be of the form

$$\boldsymbol{q} = \frac{2\pi}{a}(h,k,l) \tag{4}$$

where the Miller indices h, k, l are integers and a is a constant. Then, $f(\boldsymbol{x}) = f(\boldsymbol{x}+ma\boldsymbol{e}_1+na\boldsymbol{e}_2+oa\boldsymbol{e}_3)$ if m,n,o are arbitrary integers. This implies that f has translational periodicity with lattice vectors of magnitude a. Furthermore, if all φ_i in Eq. (1) are identical, then f is also invariant with respect to exchange of the axis and so f has the symmetry of a cubic lattice with lattice parameter a.

The above considerations imply that "spinodal" structures with translational periodicity or even cubic symmetry may be constructed by restricting the sum in Eq. (1) to a set of $\boldsymbol{q}_i$ with a given, constant value $H = \sqrt{h^2 + k^2 + l^2}$, so that $|\boldsymbol{q}| = q_0 = 2\pi H/a$ is a constant. The function f then forms a periodic repetition of identical cubic unit cells with edge length a.

Real spinodal structures emerge by the growth of a continuum with initial fluctuations including random orientation of their wave vectors [1]. It is then expected that unit cells containing many waves are more representative of real structures than those that contain few waves, which in turn suggests the use of values of H that maximize the number of individual vectors (h,k,l). In diffraction theory, this corresponds to Bragg reflections with high multiplicity. For instance, $H = \sqrt{160}$ (which implies $M \simeq 10.3$ elements per edge length, see Section 4.2 below) is only compatible with $\langle 12\,4\,0\rangle$-type vectors, which only gives 12 independent directions. By contrast, the marginally larger $H = \sqrt{161}$ is compatible with $\langle 12\,4\,1\rangle$-, $\langle 11\,6\,2\rangle$-, $\langle 10\,6\,5\rangle$- and $\langle 9\,8\,4\rangle$-type vectors and, thus, 96 independent directions. Similarly, $H = \sqrt{146}$ is compatible with $\langle 0\,5\,11\rangle$-, $\langle 1\,1\,12\rangle$-, $\langle 1\,8\,9\rangle$-, $\langle 3\,4\,11\rangle$-, and $\langle 4\,7\,9\rangle$-type vectors, leading also to 96 independent directions.

Fig. 3 illustrates the wave vector directions for $H = \sqrt{146}$, along with binarized structures created from these waves in Eq. (1). The structure in Fig. 3 (c) is based on setting $\varphi_i \equiv 0$ and exhibits full cubic symmetry. It is striking that ring-like features near the center of each face have no equivalent in experimental stochastic structures. This problem is solved by using random phase shifts φ_i in Eq. (1), see Fig. 3(b). The resulting structure compares well to experimental microstructures such as those of dealloying-made nanoporous gold. The structure now lacks the rotation- and mirror symmetry of a cubic lattice, but it retains the full translational periodicity and is suited for periodic boundary conditions.
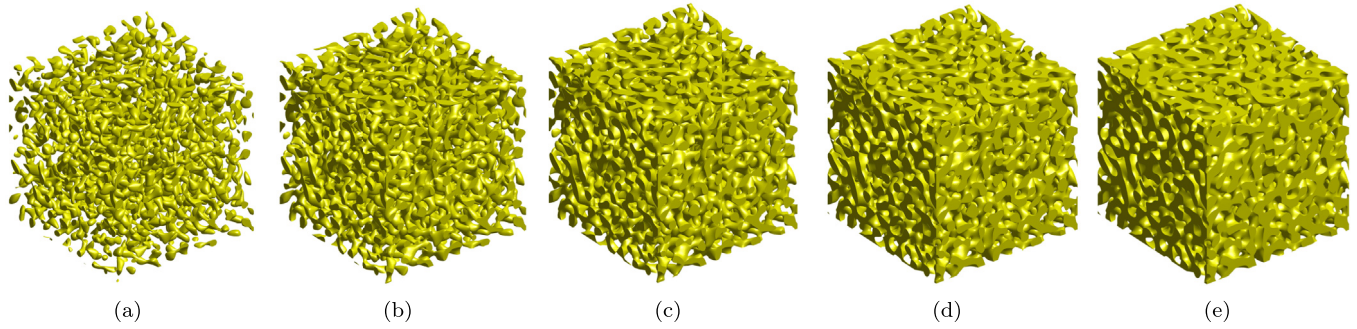
Fig. 2. Examples of microstructures generated with the level cut method for solid volume fractions of (a) 0.10, (b) 0.20, (c) 0.30, (d) 0.40, and (e) 0.50. As seen, the structure in (a) is formed of highly disjoint regions as its volume fraction is below the solid percolation threshold of $\phi_{\mathcal{B}}^{\mathrm{P}} \simeq 0.159$. Since the approach is symmetric, a structure with 0.90 volume fraction involves many disconnected and isolated voids. Volume size of 12 wavelengths and $N = 10000$ waves were used for these generations.
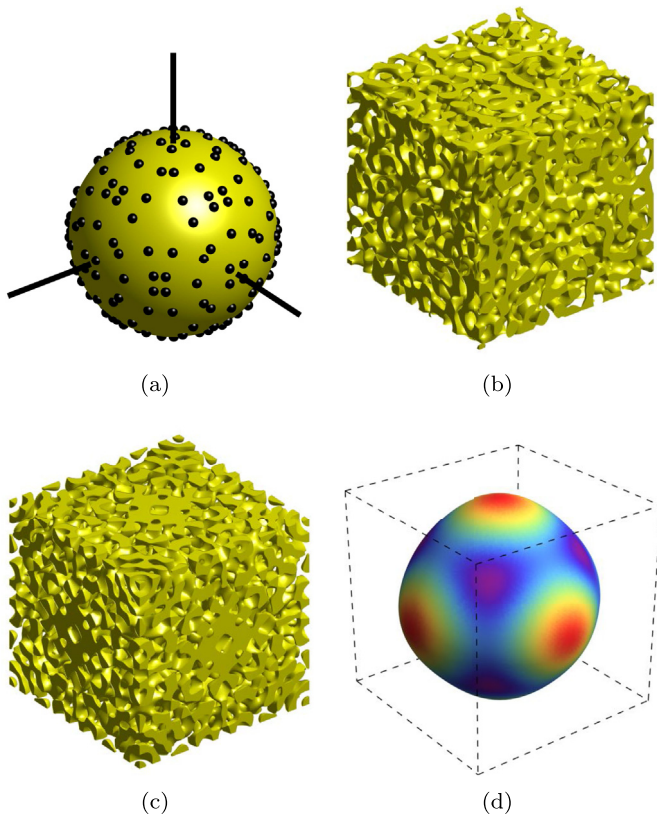

Fig. 3. Examples of binarized structures obtained from periodic fields with $H = \sqrt{h^2 + k^2 + l^2} = \sqrt{146}$. (a) Location of the 2×96 wave vectors (black dots) on a sphere in reciprocal space. Black lines refer to $\langle 100 \rangle$ directions. Note the poles with threefold, fourfold, and twofold symmetry along the $\langle 111 \rangle$, $\langle 100 \rangle$, and $\langle 110 \rangle$-type directions. (b) and (c) show a periodic microstructure without and with cubic symmetry, respectively. These structures were generated via Eq. (1) with the wave vectors $\boldsymbol{q}$ shown in part (a) and have solid fraction $\phi_{\mathcal{B}} = 0.4$. (d) Directional dependence of the effective Young's modulus of the structure shown in part (c). Note cubic symmetry; anisotropy index is $A^{\mathrm{U}} \simeq 0.02$. The structure without cubic symmetry, as given in (b), appears realistic if compared to experimental microstructures such as that of dealloying-made nanoporous gold.

4. Morphological characterization

In this section, we present explicit analytical results that characterize the morphological and topological properties of the stochastic aperiodic microstructures generated with Eq. (1) in the limit of a large number N of waves.

4.1. Solid volume fraction

For porous materials, the volume fraction of phases constitutes one of the most important morphological descriptors. Using $|\mathcal{V}| = |\mathcal{B}| + |\mathcal{P}|$, with $|\{ \bullet \}|$ denoting the volume contained in $\{ \bullet \}$, the volume fractions, $\phi_{\mathcal{B}}$ and $\phi_{\mathcal{P}}$, of the solid and pores, respectively, are defined as

$$\phi_{\mathcal{B}} := \frac{|\mathcal{B}|}{|\mathcal{V}|} \quad \text{and} \quad \phi_{\mathcal{P}} := \frac{|\mathcal{P}|}{|\mathcal{V}|}, \tag{5}$$

with $\phi_{\mathcal{B}} + \phi_{\mathcal{P}} = 1$. Given the Gaussian properties of the random function (1) the volume fraction $\phi_{\mathcal{B}}$ of the microstructure defined by Eq. (3) is given by

$$\phi_{\mathcal{B}} = \frac{1}{2}\left[1 + \mathrm{erf}\left(\frac{\xi}{\sqrt{2}}\right)\right], \tag{6}$$

where $\mathrm{erf}(x)$ denotes the error function. Inverting the equation above, we can have any desired volume fraction by setting the level cut ξ to

$$\xi(\phi_{\mathcal{B}}) = \sqrt{2}\,\mathrm{erf}^{-1}(2\phi_{\mathcal{B}} - 1), \tag{7}$$

where $\mathrm{erf}^{-1}(x)$ denotes the inverse error function. Fig. 2 shows microstructures with solid volume fractions from 0.10 to 0.50, where we can see how the microstructure with 0.10 solid volume fraction is formed of many disjoint regions. This is consistent with the percolation threshold $\phi_{\mathcal{B}}^{\mathrm{P}} \simeq 0.159$ (see below). This level of disjointness does not allow the structure to withstand applied loads.

4.2. Characteristic structure size and mean ligament diameter

Each of the components $\cos(\boldsymbol{q}_i \cdot \boldsymbol{x})$ that make up the random field $f(\boldsymbol{x})$ in Eq. (1) has the identical wavelength $\lambda = 2\pi/q_0$, which could be used as a first guess at a characteristic structure size. However, we note that a view that accounts more specifically for the properties of the random field $f(\boldsymbol{x})$ inspects the autocorrelation function, Eq. (2). The first maximum of that equation is at $q_0 r \simeq 1.23 \times 2\pi$, which measures a characteristic distance, $\tilde{L}$, between regions of maximum f. In the binarized structures, we can interpret $\tilde{L}$ to represent the characteristic structure size as measured by the mean distance between local centers of the solid or the pore space. We, thus, have

$$\tilde{L} = \alpha \frac{2\pi}{q_0}, \tag{8}$$

with $\alpha \simeq 1.23$. Experiments with dealloying-made nanoporous structures often report a characteristic size L representing a mean diameter of the solid struts or ligaments that can be perceived in medium density binarized structures such as those of Fig. 2. For structures with equal volume fraction of the two phases, symmetry suggests that $L = \tilde{L}/2$.

For periodic microstructures, in view of Eq. (8), we can take the characteristic structure size as $\tilde{L} \simeq 1.23 \times 2\pi/q_0 = 1.23a/H$. This means there are $M = a/\tilde{L} \simeq H/1.23$ microstructural elements per edge length of the unit cell, and the unit cell volume a^3 contains about $0.54H^3$ microstructural elements.

We note that another important quantity that can be used to characterize the properties of the two-phase system is the auto-correlation function, $\Gamma_2(r)$, of the solid phase. $\Gamma_2(r)$ is defined as

$$\Gamma_2(r) = \langle \mathcal{I}(\boldsymbol{x}_1)\mathcal{I}(\boldsymbol{x}_2) \rangle, \tag{9}$$

where $\mathcal{I}(\boldsymbol{x})$ is the indicator function for the solid phase which is defined via the random function as

$$\mathcal{I}(\mathbf{x}) = \begin{cases} 1, & \text{if } \boldsymbol{x} \in \mathcal{B}, \\ 0, & \text{otherwise}. \end{cases} \tag{10}$$

Furthermore, $r = |\boldsymbol{x}_1 - \boldsymbol{x}_2|$. The form of the autocorrelation function $\Gamma_2(r)$ reflects certain features of the microstructure, e.g. short range order and spatial correlation [61]. Fig. 4(a) shows plots of the numerically computed[3] normalized auto-correlation function $\Gamma_2^{\mathrm{norm}}(r) := [\Gamma_2(r) - \phi_{\mathcal{B}}^2]/[\phi_{\mathcal{B}} - \phi_{\mathcal{B}}^2]$ for volume fractions from 0.20 to 0.50. As we can see, all plots exhibit oscillations of identical periodicity for small r, hence signaling a short range order and spatial correlation in the medium generated. As expected, the mean distance between successive peaks of $\Gamma_2^{\mathrm{norm}}(r)$ is approximately $\lambda = 2\pi/q_0$, which is the same for $C_2(r)$, given by Eq. (2).

4.3. Surface area-to-volume ratio

The ratio of surface area to total (solid plus pores) volume is

$$\mathcal{S} := \frac{|\partial \mathcal{B}|}{|\mathcal{V}|}, \tag{11}$$

where $|\partial \mathcal{B}|$ denotes the total area associated with $\partial \mathcal{B}$. By considering the behavior of the two-point correlation function, $C_2(r)$, near $r = 0$, and making use of results from the scattering theory, we find an explicit formula for the surface-to-volume ratio as (see Supplementary Material for details)

$$\mathcal{S} = \frac{2q_0}{\pi\sqrt{3}} e^{-\xi^2/2}. \tag{12}$$

The ratio of surface area to solid volume is then

$$\mathcal{S}_{\mathcal{B}} = \frac{1}{\phi_{\mathcal{B}}} \frac{2q_0}{\pi\sqrt{3}} e^{-\xi^2/2}. \tag{13}$$

The dimensions of both $\mathcal{S}_{\mathcal{B}}$ and $\mathcal{S}$ are $[\mathcal{S}] = [\mathcal{S}_{\mathcal{B}}] = [1/L]$. Thus, multiplication with the characteristic size $\tilde{L}$ supplies non-dimensionalization and provides quantities devoid of volume and length scale differences. Fig. 4(b) shows the plots of $\mathcal{S}_{\mathcal{B}}(\phi_{\mathcal{B}})$ and $\mathcal{S}(\phi_{\mathcal{B}})$ as given by the above relations, where we can see, as

---

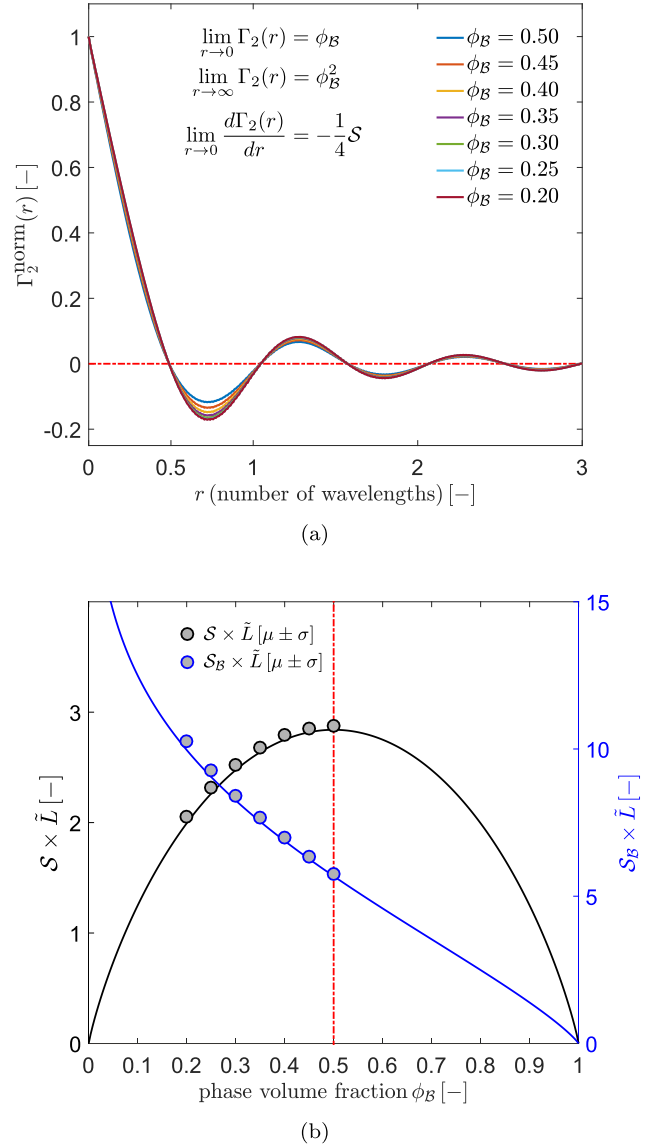[3] Details of the computations can be found in the Supplementary Material.

Fig. 4. (a) Numerically generated normalized auto-correlation function $\Gamma_2^{\mathrm{norm}}(r) := [\Gamma_2(r) - \phi_{\mathcal{B}}^2]/[\phi_{\mathcal{B}} - \phi_{\mathcal{B}}^2]$. 2D binary sections of 15 3D random generations are used for each volume fraction. Plots show significant oscillations which is a sign of regularity in the microstructure. The mean distance in successive peaks of both of the functions is approximately $\lambda = 2\pi/q_0$. (b) Scaled specific surface areas, $\mathcal{S}$ per total volume and $\mathcal{S}_{\mathcal{B}}$ per solid volume, versus solid phase fraction plots. Continuous lines are analytical predictions given by Eqs. (12) and (13), filled symbols correspond to numerical results for specific surface areas from the relation $\lim_{r\to 0} d\Gamma(r)/dr = -1/4\,\mathcal{S}$ (see Supplementary Material) where data is presented as mean value μ (dots) and standard deviation σ (error bars) from analysis of 15 random realizations.

expected, that $\mathcal{S}_{\mathcal{B}}$ decreases monotonically, and $\mathcal{S}$ is symmetric with respect to $\phi_{\mathcal{B}} = 0.50$ with a maximum at this point. The discrete points in Fig. 4(b) correspond to the numerical values computed from the auto-correlation function $\Gamma_2(r)$ of the generated microstructures (see the inset of Fig. 4(a) and the Supplementary Material for details on how $\Gamma_2(r)$ is related to $\mathcal{S}$), observing an excellent agreement with the analytical predictions.

4.4. Average curvatures and percolation-to-cluster transition

In differential geometry, the product of principal curvatures κ_1

and κ_2 yields the Gaussian curvature of a surface at a point as $\kappa_{\mathrm{g}} = \kappa_1\kappa_2$, whereas the mean curvature is defined as $\kappa_{\mathrm{m}} = [\kappa_1 + \kappa_2]/2$. For the Gaussian random field of Eq. (1), the average Gaussian curvature and the average mean curvature are [64]

$$\langle\kappa_{\mathrm{g}}\rangle = \frac{q_0^2}{6}\left[\xi^2 - 1\right] \quad \text{and} \quad \langle\kappa_{\mathrm{m}}\rangle = -\xi\frac{q_0}{2}\sqrt{\frac{\pi}{6}}, \quad (14)$$

respectively, where we use the curvature definition of $\kappa_1 > 0$ and $\kappa_2 > 0$ for a solid (convex) ellipsoid. Table 1 shows tabulated values of surface area-to-volume ratios, average Gaussian and average mean curvature, rescaled with the characteristic structure size $\tilde{L}$ given by Eq. (8) as a function of the solid volume fraction. Fig. 5(a) shows the variation of average scaled Gaussian and mean curvatures with the solid volume fraction, along with examples of microstructures.

We observe that the Gaussian curvature crosses zero at two critical points, namely $\phi_{\mathcal{B}} = \phi_{\mathcal{B}}^{\mathrm{p}} \approx 0.159$ and $\phi_{\mathcal{B}} = 1 - \phi_{\mathcal{B}}^{\mathrm{p}} \approx 0.841$, which correspond to the solid percolation threshold and pore percolation threshold, respectively. Based on these values, we can identify four distinct types of microstructure: (i) $\phi_{\mathcal{B}} < \phi_{\mathcal{B}}^{\mathrm{p}}$, the microstructure is formed of disjoint solid phases (convex ellipsoids) with local curvatures $\kappa_1 > 0$ and $\kappa_2 > 0$ which gives $\kappa_{\mathrm{m}} > 0$ and $\kappa_{\mathrm{g}} > 0$, (ii) $\phi_{\mathcal{B}}^{\mathrm{p}} < \phi_{\mathcal{B}} < 0.50$, thin and long saddle-like ligament formations with sharp positive local curvature ($\kappa_1 > 0$) at their sections but mild negative local curvature ($\kappa_2 < 0$) along their lengths dominate with $|\kappa_1| > |\kappa_2|$ resulting in $\kappa_{\mathrm{m}} > 0$ and $\kappa_{\mathrm{g}} < 0$, (iii) $0.50 < \phi_{\mathcal{B}} < 1 - \phi_{\mathcal{B}}^{\mathrm{p}}$, thick and short saddle-like ligament formations with mild positive local curvature ($\kappa_1 > 0$) at their sections but sharp negative local curvature ($\kappa_2 < 0$) along their lengths dominate with $|\kappa_1| < |\kappa_2|$ resulting in $\kappa_{\mathrm{m}} < 0$ and $\kappa_{\mathrm{g}} < 0$, (iv) $\phi_{\mathcal{B}} > 1 - \phi_{\mathcal{B}}^{\mathrm{p}}$, disjoint pores (concave ellipsoids) characterize the microstructure with $\kappa_1 < 0$ and $\kappa_2 < 0$, and so $\kappa_{\mathrm{m}} < 0$ and $\kappa_{\mathrm{g}} > 0$.

We also note that only the 0.50 vol fraction case has zero average mean curvature, which agrees well with the results reported in Ref. [68]. At this point the average Gaussian curvature has a minimum. The Gaussian curvature is symmetric with respect to $\phi_{\mathcal{B}} = 0.50$, whereas the mean curvature is instead showing a monotonic decrease with increasing phase volume fraction. These trends are in agreement with experimental studies presented in the literature. Fujita et al. [27] measured near zero mean curvature for nanoporous gold samples of $\phi_{\mathcal{B}} \simeq 0.50$. A positive average mean curvature was reported by Rösner et al. [26] for nanoporous gold with a lower metal volume fraction of $\phi_{\mathcal{B}} \simeq 0.24$.

4.5. Genus

The genus G of a surface describes its connectivity; it can be understood as the number of continuous tunnels or loops in the structure. For instance, a sphere, donut and pretzel have the genus 0, 1, and 2, respectively. By making use of the Gauss-Bonnet

Table 1
Dependence of surface area-to-(bulk) volume ratio, average Gaussian and average mean curvature on porosity. For $\phi_{\mathcal{B}} = 0.10$, the condition $\langle\kappa_{\mathrm{g}}\rangle > 0$ signals a dominating amount of disjoint lumps of material.

$\phi_{\mathcal{B}}$	ξ	$\mathcal{S} \times \tilde{L}$	$\mathcal{S}_{\mathcal{B}} \times \tilde{L}$	$\langle\kappa_{\mathrm{g}}\rangle \times \tilde{L}^2$	$\langle\kappa_{\mathrm{m}}\rangle \times \tilde{L}$
0.1	−1.2816	1.2496	12.4959	6.3945	3.5834
0.2	−0.8416	1.9934	9.9670	−2.9035	2.3533
0.3	−0.5244	2.4757	8.2522	−7.2170	1.4663
0.4	−0.2533	2.7509	6.8771	−9.3156	0.7084
0.5	0	2.8406	5.6811	−9.9545	0
0.6	0.2533	2.7509	4.5848	−9.3156	−0.7084
0.7	0.5244	2.4757	3.5366	−7.2170	−1.4663
0.8	0.8416	1.9934	2.4917	−2.9035	−2.3533
0.9	1.2816	1.2496	1.3884	6.3945	−3.5834
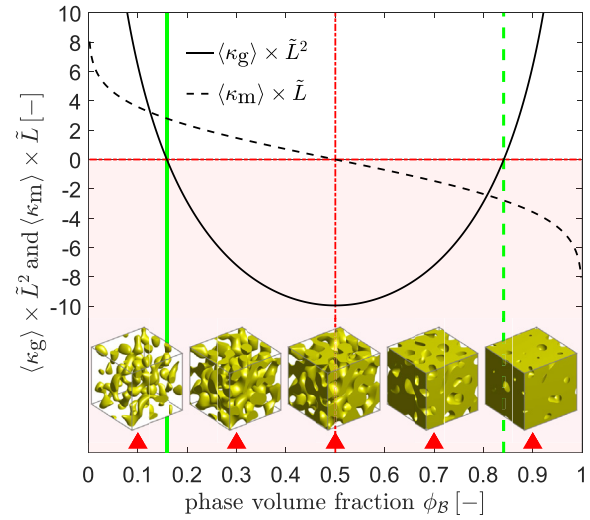
(a)
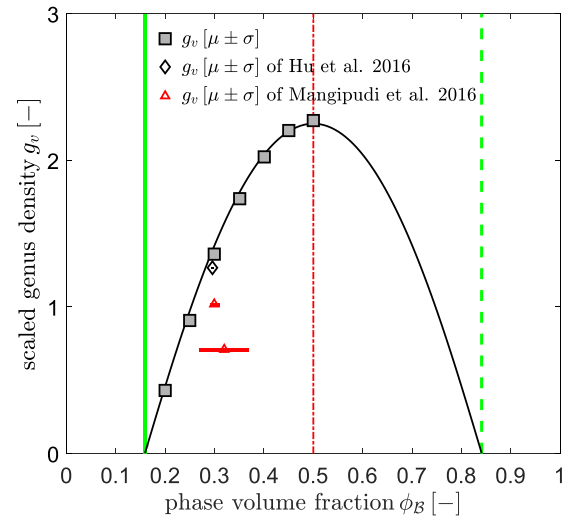
(b)

Fig. 5. (a) Scaled average Gaussian and mean curvature plots. The solid green line depicts the solid percolation threshold with $\phi_{\mathcal{B}} = \phi_{\mathcal{B}}^{\mathrm{p}} \approx 0.159$ whereas the dashed green line depicts the pore percolation threshold with $\phi_{\mathcal{B}} = 1 - \phi_{\mathcal{B}}^{\mathrm{p}} \approx 0.841$. (b) Scaled genus per volume versus solid phase fraction plots. Continuous line corresponds to the analytical expression (16), filled symbols are the numerical results for genus that are obtained from Betti number computations (see Supplementary Material), unfilled symbols correspond to experimental values from Refs. [23,24], which have been adapted to the characteristic length scale used in this work (see Appendix A). Here, data is presented as mean value μ (dots) and standard deviation σ (error bars) from experiments or current analysis of 15 random realizations. (For interpretation of the references to colour in this figure legend, the reader is referred to the web version of this article.)

theorem and the known Gaussian curvature per unit volume, it is possible to obtain the following expression for the genus per unit volume, G_v, in our random field microstructures (see Supplementary Material for details):

$$G_v = \frac{1}{12\pi^2}\frac{q_0^3}{\sqrt{3}}\left[1 - \xi^2\right]e^{-\xi^2/2}. \quad (15)$$

The above relation depends on the characteristic length scale of the microstructure through q_0. To study a non-dimensional quantity we rescale the genus per volume with the characteristic

structure size $\tilde{L}$, see Eq. (8), to obtain the scaled genus per volume:

$$g_v = G_v \times \tilde{L}^3 = \frac{2\pi\alpha^3}{3\sqrt{3}}\left[1 - \xi^2\right]e^{-\xi^2/2}. \qquad (16)$$

Fig. 5(b) shows the prediction of Eq. (16) for the scaled genus versus solid fraction. Similarly to the average curvatures analysis from the previous section, Eqs. (15) and (16) also predict a topological transition at a finite phase fraction. The genus vanishes at $|\xi| = 1$, which according to Eq. (6), corresponds to $\phi_{\mathcal{B}} = \phi_{\mathcal{B}}^{\mathrm{P}} \simeq 0.159$ for $\xi = -1$. For phase fractions $\phi_{\mathcal{B}} > \phi_{\mathcal{B}}^{\mathrm{P}}$, the structure may be understood as a percolating and multiply interconnected network. At lesser $\phi_{\mathcal{B}}^{\mathrm{P}}$, connectivity is lost and the structure becomes an array of isolated clusters with genus zero. The phase fraction $\phi_{\mathcal{B}}^{\mathrm{P}}$ thus marks the percolation-to-cluster transition, below which Eq. (16) is no longer applicable. On the other hand, at $\phi_{\mathcal{B}} \simeq 0.841$, which corresponds to $\xi = 1$, there is the topological transition above which the structure contains isolated voids.

To compute the genus numerically we use the fact that the genus is related to the second Betti number as $G = B_1/2$. By numerically computing the second Betti number per unit volume, $B_{1,v}$, we obtain the genus density as $G_v = B_{1,v}/2$. Fig. 5(b) illustrates the excellent agreement between the analytical and numerical results.

Experimental findings on the topological properties of nanoporous gold are, in contrast to the mechanical properties, rather limited. Results of an experimental quantitative study based on 3D-focused ion beam tomography applied to as-dealloyed and isothermally annealed nanoporous gold samples [24] and those of [69] from 3D-focused ion beam tomography applied to two nanoporous gold samples using the improved-wedge are depicted in Fig. 5(b) considering the reported error margins.[4] As seen in the plot, the scaled genus density reported in Ref. [24] is in a very good agreement with our prediction being about $\simeq 0.91$ of it. With less agreement, the results of [69] correspond to $0.45 - 0.71$ of our predictions.

5. Elastomechanical characterization

5.1. Homogenization and effective mechanical property determination

Let $\boldsymbol{u} : \mathcal{B} \times \mathcal{R}_+ \to \mathcal{R}^3$ denote the displacement field at $\boldsymbol{x} \in \mathcal{B}$ at time $t \in \mathcal{R}_+$. The microscopic strain tensor $\boldsymbol{\varepsilon}$ is defined as $\boldsymbol{\varepsilon} := \mathrm{sym}(\nabla\boldsymbol{u})$. In absence of dynamic effects and body forces, micro-equilibrium state requires $\mathrm{div}\,\boldsymbol{\sigma} = \boldsymbol{0}$ in $\mathcal{B}$ where $\boldsymbol{\sigma}$ is the microscopic Cauchy stress tensor. Considering linear and infinitesimal elasticity, we introduce the constitutive relation at the microstructure $\boldsymbol{\sigma} = \mathbb{C} : \boldsymbol{\varepsilon}$ in $\mathcal{B}$ where $\mathbb{C}$ is the elastic constitutive tensor. For elastic isotropy at microscale, we have $\mathbb{C} = 3K\,\mathbb{I}^{\mathrm{vol}} + 2\mu\,\mathbb{I}^{\mathrm{dev}}$ where $\mathbb{I}^{\mathrm{vol}} = 1/3\,\boldsymbol{1} \otimes \boldsymbol{1}$, $\mathbb{I}^{\mathrm{dev}} = \mathbb{I} - \mathbb{I}^{\mathrm{vol}}$ with $\mathbb{I} = 1/2[\boldsymbol{1}\overline{\otimes}\boldsymbol{1} + \boldsymbol{1} \otimes \boldsymbol{1}]$. Here, K and μ are the bulk and the shear moduli, respectively. μ is the second-order identity tensor.

Analogous to the microscale, we assume that the effective elasticity tensor $\mathbb{C}^{\star}$ at macroscale relates the macroscopic stress tensor $^{\mathrm{M}}\boldsymbol{\sigma}$ to macroscopic strain tensor $^{\mathrm{M}}\boldsymbol{\varepsilon}$ at $^{\mathrm{M}}\boldsymbol{x}$ linearly viz. $^{\mathrm{M}}\boldsymbol{\sigma} = \mathbb{C}^{\star}{:}^{\mathrm{M}}\boldsymbol{\varepsilon}$ in $^{\mathrm{M}}\mathcal{B}$ with $^{\mathrm{M}}\boldsymbol{\sigma} = 1/|\mathcal{V}|\int_{\mathcal{B}}\boldsymbol{\sigma}\mathrm{d}V$ for the porous microstructure.[5] Definition of the components of $\mathbb{C}^{\star}$ requires six independent loading cases under periodic boundary conditions, see

Supplementary Material.

5.2. Quantification of the degree of anisotropy and aggregate properties

In its limiting behavior for a large number N of waves and a large volume, the Gaussian random field of our analysis is isotropic, and for the current particular case this property implies elastic isotropy.[6] Thus, an assessment whether numerical realizations are representative can be based on their degree of mechanical anisotropy. An interpretation of the elasticity constants is in terms of Young's modulus E, i.e., the sensitivity of stress increment to strain increment along the loading direction under uniaxial state of stress. Assuming loading along the unit direction $\boldsymbol{m}$ the corresponding effective Young's modulus $E_{\boldsymbol{m}}^{\star}$ is computed as

$$E_{\boldsymbol{m}}^{\star} = \frac{1}{[\boldsymbol{m}\otimes\boldsymbol{m}] : \mathbb{S}^{\star} : [\boldsymbol{m}\otimes\boldsymbol{m}]}, \qquad (17)$$

where $\mathbb{S}^{\star} = [\mathbb{C}^{\star}]^{-1}$ is the compliance tensor.[7] By plotting $E_{\boldsymbol{m}}^{\star}$ for all $\boldsymbol{m}$ one can develop an understanding regarding the directional dependence of elasticity.

For the quantification of the extent of anisotropy in the material, various measures exist, e.g., for cubic crystals, Zener [71] introduced an anisotropy index. However this index is restricted to cubic crystals and lacks universality [72]. Thus, we use the universal anisotropy index [72], which overcomes these limitations:

$$A^{\mathrm{U}} = \frac{K_{\mathrm{V}}}{K_{\mathrm{R}}} + 5\frac{\mu_{\mathrm{V}}}{\mu_{\mathrm{R}}} - 6 \geq 0. \qquad (19)$$

Here, K and μ represent isotropicized single crystal elasticity shear and bulk moduli which are obtained through assignment of the single crystal orientation uniformly on a sphere of 3D distributions. The subsequent ensemble averaging over the unit sphere[8] is denoted by $\langle\{\bullet\}\rangle_\circ$, so that the elastic constitutive tensor and the compliance tensor are given as

$$\begin{aligned} \mathbb{C}_{\mathrm{V}}^{\star} &= \langle\mathbb{C}^{\star}\rangle_\circ = 3K_{\mathrm{V}}\mathbb{I}^{\mathrm{vol}} + 2\mu_{\mathrm{V}}\mathbb{I}^{\mathrm{dev}}, \\ \mathbb{S}_{\mathrm{R}}^{\star} &= \langle\mathbb{S}^{\star}\rangle_\circ = \frac{1}{3K_{\mathrm{R}}}\mathbb{I}^{\mathrm{vol}} + \frac{1}{2\mu_{\mathrm{R}}}\mathbb{I}^{\mathrm{dev}}, \end{aligned} \qquad (22)$$

where R and V stand for Reuss and Voigt estimates, respectively. $A^{\mathrm{U}} = 0$ for isotropic materials, as in the case of macroscopic

---

[6] Statistical isotropy does not necessarily result in mechanical isotropy [61].

[7] Poisson's ratio, where the direction of observation $\boldsymbol{m}_\perp$ is perpendicular to the loading direction $\boldsymbol{m}$ can be given as [70].

$$\nu_{(\boldsymbol{m},\boldsymbol{m}_\perp)}^{\star} = -\frac{[\boldsymbol{m}_\perp\otimes\boldsymbol{m}_\perp] : \mathbb{S}^{\star} : [\boldsymbol{m}\otimes\boldsymbol{m}]}{[\boldsymbol{m}\otimes\boldsymbol{m}] : \mathbb{S}^{\star} : [\boldsymbol{m}\otimes\boldsymbol{m}]}. \qquad (18)$$

[8] Spherical averaging reads.

$$\langle\{\bullet\}\rangle_\circ = \frac{1}{4\pi}\int_0^{2\pi}\int_0^{\pi}\{\bullet\}(\Theta,\Phi)\sin\Theta\mathrm{d}\Theta\mathrm{d}\Phi. \qquad (20)$$

Numerically, this can be realized considering $M > 200$ points as unit directors of a Fibonacci tiling, with $\{\bullet\}_{(i)} = \{\bullet\}(\Theta_i, \Phi_i)$ where $i = 1, 2, 3, ..., M$. Then

$$\langle\{\bullet\}\rangle_\circ \simeq \frac{1}{M}\sum_{i=1}^{M}\{\bullet\}_{(i)}. \qquad (21)$$

As it is done in this study, for computation of elastic aggregate properties, one can also make use of the invariance properties of the elastic constitutive tensor [73], see Supplementary Material

---

[4] For the details of how these reported results are converted to our scaling convention, the reader is referred to Appendix A.

[5] Due to the porous structure $^{\mathrm{M}}\boldsymbol{\varepsilon} \neq 1/|\mathcal{V}|\int_{\mathcal{B}}\boldsymbol{\varepsilon}\mathrm{d}V$. Thus, macroscopic strains are computed through control nodes of the volume element.

response of nanoporous gold, and $A_\mathrm{U} > 0$ increases with increasing level of anisotropy[9]

6. Results and discussion

6.1. On the topological properties

As pointed out in Ref. [23], microstructures that appear similar to that of nanoporous gold can exhibit variations in apparent scaled genus by one order of magnitude. The observation that the scaled genus of our random field microstructure matches experimental reconstructions of nanoporous gold to the factor two or better may thus be considered as promising. It is also significant that the experimental structures have lesser g_v than our model. This is consistent with the trend — pointed out by Mameka et al. in Ref. [13] — for g_v in spinodal-like structures such as nanoporous gold to decrease during spontaneous coarsening. That trend implies that the early-stage spinodal structure of Ref [1], which underlies the present model, represents the maximum scaled genus for the respective volume fraction. Lesser g_v can be expected when spinodal microstructures were prepared by Phase Field or Kinetic Monte Carlo simulation, since those simulation approaches follow the evolution of the microstructure into the later stages of spinodal decomposition, where the phase separation is nearly complete. That evolution may already involves coarsening and, hence, reduction in g_v.

According to Ref [13], lesser g_v may specifically be expected in experiments when samples were allowed to undergo spontaneous coarsening during corrosion, during storage at room temperature, or during deliberate annealing treatments. It is this reasoning that prompts us to limit the comparison between experiment and the connectivity or stiffness data of our model to experimental samples that were in their as-prepared state. Coarsened samples are excluded from the comparison because of their likely lesser scaled genus.

6.2. Determination of the RVE size for mechanical properties

In the following, we present details on how to choose the model parameters in order to generate representative microstructures. An RVE is a volume of material whose effective behavior is representative of that of the material as a whole. Although for a homogeneous fictitious material the size of the RVE is irrelevant, in order to satisfy statistical representativeness the RVE must contain a sufficiently large volume for heterogeneous materials. This size should be sufficiently large compared to the characteristic microstructural length scales of the material, here the diameter and length of the nanoporous ligaments, and still be sufficiently small compared to the characteristic length of a macroscopic sample [74]. In order to determine an appropriate RVE size, we conducted a set of
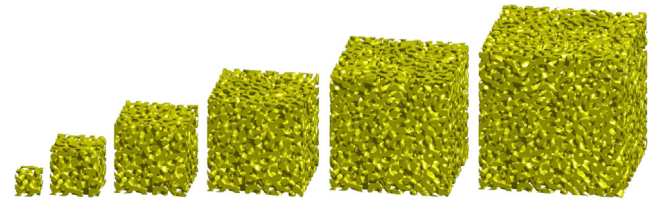

Fig. 6. Volume elements with edge sizes of (left to right) 3, 6, 9, 12, 15 and 18 wavelengths. $\phi_\mathcal{B} = 0.40$. The corresponding finite element models used $32 \times 32 \times 32$, $64 \times 64 \times 64$, $96 \times 96 \times 96$, $128 \times 128 \times 128$, $160 \times 160 \times 160$ and $192 \times 192 \times 192$ voxels, so that the voxel size is constant.

simulations considering various volume element sizes, see Fig. 6, and computed the corresponding macroscopic properties. In order to collect sufficient statistical information, 15 realizations were generated for each volume element size.

Unless otherwise stated, the results are for aperiodic structures. The homogenization scheme is computationally implemented with the finite element method. As detailed in Section 2, we use a fixed[10] wave number $|\boldsymbol{q}| = q_0$ and we present the volume element sizes in terms of number of wavelengths. We use 3D full integration first order trilinear finite elements through voxelization[11] of the domain. All reported results use fixed sized voxels, where the voxel size is determined through a mesh convergence analysis, considering the computational memory and time requirements of the structures with higher solid volume fractions within the statistical computations. Since no size dependent constitutive phenomena is used during modeling, the computed mechanical properties are equally valid for any ligament size. The underlying statistical properties require the number of waves approaching infinity. As explained earlier $N = 10000$ waves are sufficient in our applications considering isotropy of the field. Thus, for all applications with aperiodic structures we use $N = 10000$.

Motivated by experiments with nanoporous gold made by dealloying (see below), we consider $\phi_\mathcal{B}$ in the range of $0.20-0.50$. The crystal lattice of gold has cubic symmetry and is elastically anisotropic. In the interest of conciseness, this elastic anisotropy is ignored in the current study. We assume isotropic elasticity of the solid phase and, for contact with the experiments, use the parameters of polycrystalline gold for the Young's modulus $E_\mathcal{B}$ and for the Poisson's ratio $\nu_\mathcal{B}$ of the solid phase: $E_\mathcal{B} = 79$ GPa and $\nu_\mathcal{B} = 0.44$ [82].

The macroscopic Young's moduli and Poisson's ratios are now discussed. Since the macroscopic elastic isotropy is not a priori satisfied for all volume element sizes, the computations are presented in terms of aggregate macroscopic elastic properties $E_\mathrm{HVR}^\star$ (top) and $\nu_\mathrm{HVR}^\star$ as depicted in Fig. 7 for 0.20 and 0.50 phase volume fractions. Aggregate elastic properties are derived from Voigt and

---

[9] The origin of the index then stems from the contraction

$$\mathbb{C}_\mathrm{V}^\star :: \mathbb{S}_\mathrm{R}^\star = \langle \mathbb{C}^\star \rangle_\circ :: \langle \mathbb{S}^\star \rangle_\circ = \frac{K_\mathrm{V}}{K_\mathrm{R}} + 5\frac{\mu_\mathrm{V}}{\mu_\mathrm{R}}, \qquad (23)$$

which is six if the crystal is locally isotropic [72].

[10] For a fixed wave number, the microstructures are not triply periodic unless the periodicity condition is explicitly imposed, see Section 3.2. In our study, we mainly consider the more general aperiodic ones. Still, we apply periodic boundary conditions due to their superior convergence properties. This is especially important for multiphase composites with highly contrasted phase mechanical properties for which the kinematic uniform boundary conditions overestimates the effective properties at reasonable volume element sizes. For more discussions on the use of periodic boundary conditions for aperiodic microstructures in homogenization the reader is referred to, e.g., [25,75—80].

[11] Voxel based approaches are problematic for physical problems dependent on surface area (such as surface elasticity, thermal transport, electromagnetic radiation and chemical diffusion) as the surface area is appreciably overestimated [81]. This overestimation cannot be remedied by mesh refinement (e.g., for a sphere meshed as cubic voxels as the element side length over radius of sphere ratio tends to zero, the ratio of the voxel mesh surface area to that of a perfect sphere will tend to $3/\sqrt{3} \approx 1.73$ - in other words, in the limit, the surface area is overestimated by more than 0.70). As we do not study surface area dependent problems, the voxel mesh is fully sufficient for the purpose of this work.
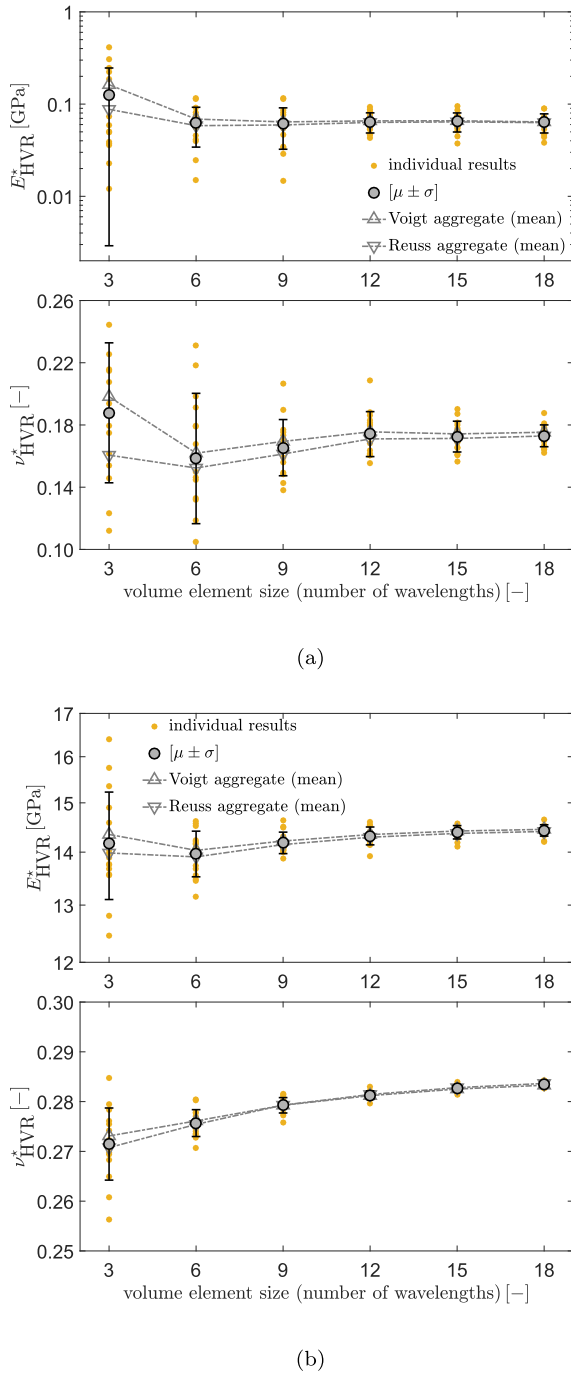
Fig. 7. Effective aggregate properties for Young's modulus $E_{HVR}^{\star}$ (top) and effective Poisson's ratio $v_{HVR}^{\star}$ (bottom) versus volume element (VE) size for (a) 0.20 solid volume fraction and (b) 0.50 solid volume fraction with corresponding Voigt and Reuss aggregate property bounds (see Supplementary Material). As anticipated, with increasing volume element size, the properties converge to their effective values. A convergence of the effective properties is judged for the volume element size of 12 wavelengths with corresponding values of $E^{\star} = 0.0644 \pm 0.0159$ GPa and $v^{\star} = 0.1741 \pm 0.0145$ for 0.20, and $E^{\star} = 14.322 \pm 0.179$ GPa and $v^{\star} = 0.2813 \pm 0.0009$ for 0.50 solid volume fraction. Data is presented as mean value μ (dots) and standard deviation σ from analysis of 15 random realizations.

Reuss aggregate property bounds of the bulk and shear moduli (see Supplementary Material for details). For each volume element size, 15 realizations are used. The means of the aggregate macroscopic Young's moduli and Poisson's ratios swiftly converge to their

effective values with growing volume element size with a narrower error bar. The aggregate effective Young's modulus $E_{HVR}^{\star}$ and aggregate effective Poisson's ratio $v_{HVR}^{\star}$ are well converged as the volume element size reaches 12 wavelengths. Therefore, 12 wavelengths is identified as the RVE size. At this point, $E_{HVR}^{\star} = 0.0644 \pm 0.0159$ GPa and $v_{HVR}^{\star} = 0.1741 \pm 0.0145$ for 0.20, and $E_{HVR}^{\star} = 14.322 \pm 0.179$ GPa and $v_{HVR}^{\star} = 0.2813 \pm 0.0009$ for 0.50 solid volume fraction.[12] The scatter in the results for 0.50 solid volume fraction is smaller than at 0.20. Most remarkably, the effective Young's modulus for the former is nearly two orders of magnitude larger than for the latter.

For sufficiently large volume element size, the elastic behavior in the computations approaches the isotropy of the random field. We verify this in 1080 simulations whose results are demonstrated in Figs. 8 and 9. Since $A^U = 0$ represents isotropy and $A^U \geq 0$, one anticipates decreasing universal anisotropy index with increasing volume element size. As depicted in Fig. 8, for both volume fractions, our results fall below 0.5 and, thus, sufficiently meet isotropy expectation if the volume element size is 12 wavelengths or larger. For 0.20 and 0.50 solid volume fractions, the anisotropy indices read 0.2270 ± 0.0890 and 0.0221 ± 0.0077, respectively, where the latter structure has about ten times less anisotropy. Fig. 9 demonstrates the volume element size influence on the directional dependence of normalized Young's modulus for 0.20 and 0.50 solid volume fractions. Here, the results are ordered vertically from minimum (bottom) to maximum anisotropy index (top). Plots of the first column of Fig. 9(a), that is for the volume element size of 3 wavelengths, signal a substantial deviation from isotropy. Here, the load transfer along directions where there is lack of percolation of the matter is highly disturbed. Thus, the stiffness along such directions is computed to be quite small and this creates an extreme polarity in the directional response of material. As the volume element size gets larger, the surface morphologies tend to that of a sphere. For 0.50 solid volume fraction, this tendency is much faster. Even for the smallest volume element size, no extreme polarization is observed. At this solid volume fraction, the solid and pore phases are symmetric in content, and percolation prevails.

In addition to the stochastic aperiodic structures, we also considered periodic structures as described in Section 3.2. The effective elastic properties of periodic, but not cubic symmetric, structures were computed based on 15 realizations satisfying $H = \sqrt{146}$, hence the volume element edge length 12 wavelengths. These results are presented in the subsequent section.

6.3. Scaling law for elastic properties

As demonstrated in the preceding section, by using a RVE size of 12 wavelengths or higher, one can sufficiently reduce the gap between Voigt and Reuss aggregate property bounds and the universal anisotropy index. Therefore, aggregate effective elastic properties in fact represent effective elastic properties of the medium. This allows us to drop the subscript HVR and concisely use $E^{\star}$ and $v^{\star}$ while denoting the effective Young's modulus and Poisson's ratio, respectively. The variation of the converged effective Young's modulus results from our study with solid fraction is displayed by the circles in Fig. 10(a). The mean values are obtained using computations conducted over 15 realizations. The first notable observation is that our periodic structures with 96 waves give sensibly the identical behavior as our aperiodic ones with 10000 waves. The mutual consistency supports the validity of both approaches.

---

[12] Although not shown as plots, we determined $K_{HVR}^{\star} = 0.0329 \pm 0.0077$ GPa and $\mu_{HVR}^{\star} = 0.0275 \pm 0.0069$ GPa for 0.20, and $K_{HVR}^{\star} = 10.915 \pm 0.1763$ GPa and $\mu_{HVR}^{\star} = 5.5888 \pm 0.0665$ GPa for 0.50 solid volume fraction.
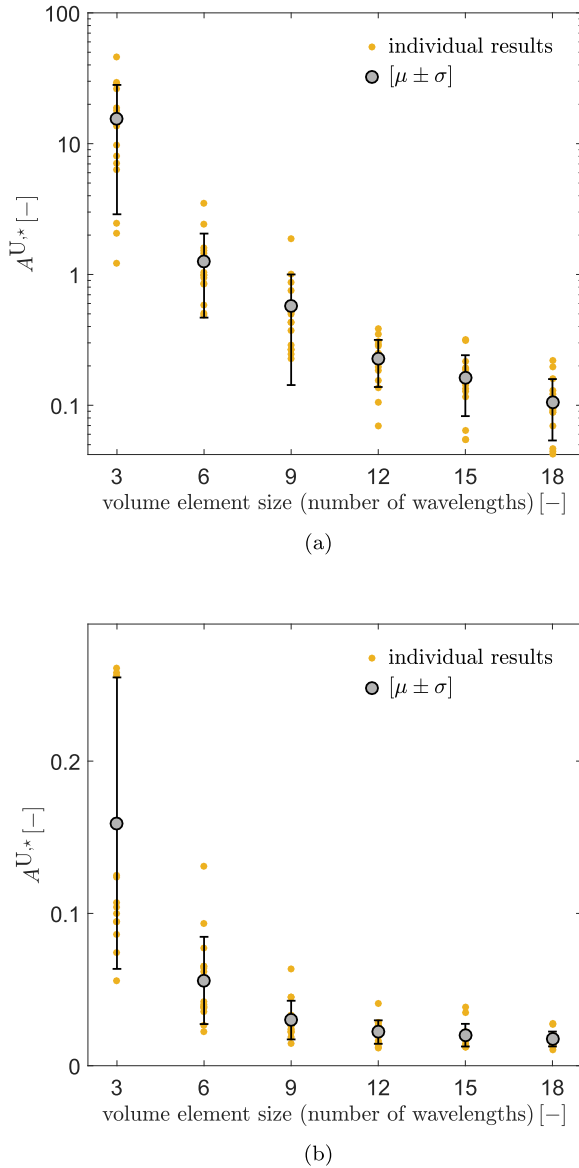
(a)

(b)

Fig. 8. Convergence of macroscopic universal anisotropy index with increasing volume element size for (a) 0.20 and (b) 0.50 solid volume fraction. Mean values decay fast with corresponding error bars getting smaller as the volume element size increases. For a 0.20 solid volume fraction smaller volume element sizes result in a relatively higher anisotropic response. Data is presented as mean value μ (dots) and standard deviation σ from analysis of 15 random realizations.

It is also remarkable that, between solid fractions of 0.50 and 0.20, $E^{\star}$ drops by more than two orders of magnitude. As a reference, the dashed line in the figure represents the Gibson-Ashby scaling law for the effective elasticity of open cell foams [6,38],

$$\frac{E^{\star}}{E_{\mathcal{B}}} = C_1 \phi_{\mathcal{B}}^2, \tag{24}$$

where we choose $C_1 = 1$ as the value that is typically used when the scaling law is compared to experimental data for nanoporous gold [8,10,13—15,83]. The figure makes it strikingly apparent that the steep variation of $E^{\star}$ with the solid fraction is not compatible with the much more shallow power law scaling of the Gibson-Ashby law.

In a finite element simulation study of the elastic properties of stochastic microstructures, Roberts and Garboczi [25] propose a scaling law that explicitly accounts for the presence of a percolation threshold given by $E^{\star} = E_{\mathcal{B}}[[\phi_{\mathcal{B}} - \phi_0]/[1 - \phi_0]]^m$. This motivates our plot of the normalized $E^{\star}$ versus $[\phi_{\mathcal{B}} - \phi_{\mathcal{B}}^{\mathrm{P}}]/[1 - \phi_{\mathcal{B}}^{\mathrm{P}}]$ in Fig. 10(b). As derived in Section 4.4, $\phi_{\mathcal{B}}^{\mathrm{P}} = [1 + \mathrm{erf}(2^{-1/2})]/2 \simeq 0.159$ is the percolation threshold of our random field microstructures. Since the linear regression does not extrapolate to $E^{\star} = E_{\mathcal{B}}$ at $\phi_{\mathcal{B}} = 1$, we are led to propose a modified version of the Roberts-Garboczi scaling law in the form

$$\frac{E^{\star}}{E_{\mathcal{B}}} = C_2 \left[\frac{\phi_{\mathcal{B}} - \phi_{\mathcal{B}}^{\mathrm{P}}}{1 - \phi_{\mathcal{B}}^{\mathrm{P}}}\right]^m. \tag{25}$$

If averaged over the data for periodic and aperiodic structures, the linear regression suggests $C_2 = 2.03 \pm 0.16$ and $m = 2.56 \pm 0.04$. The excellently linear behavior of our effective Young's moduli in the representation of Fig. 10(b) provides convincing evidence for the stiffness to vanish along with the topological genus at precisely the percolation limit. This differs from the statement by Roberts and Garboczi[13] who, exploring structures in a more restricted range of phase fractions and working with their original scaling equation, suggested that $E^{\star}$ may vanish at a solid fraction which is above the percolation limit [25].

The fit to our numerical results with Eq. (25) is reproduced in Fig. 10(a) as the solid line. Also shown (noncircular symbols) is experimental data from Refs. [13—15],[83] for the reduced effective Young's modulus of the material that motivates our study, nanoporous gold, with different solid fraction. That data underlines the finding — highlighted in the experimental studies and confirmed by atomistic simulation [19,55,56] of nanoporous gold — that the material is generally more compliant than predicted by the Gibson-Ashby law. Our compilation of the experimental data emphasizes that this deviation systematically increases as the solid fraction is reduced. Most remarkable, however, is the excellent agreement of our simulations with experiments.

The variation of the converged effective Poisson's ratio results from our study with solid fraction is displayed by the circles in Fig. 11. Here, the noncircular symbols show experimental data for the elastic Poisson's ratio of nanoporous gold from Refs. [15,16]. It is seen that our results agree, within error bars, with the experiment. The agreement confirms the notion that our random field microstructure provides a faithful model for the structure of dealloying-made nanoporous gold. In comparison with the Young's modulus, $\nu^{\star}$ exhibits a more moderate variation with $\phi_{\mathcal{B}}$. We found a highly linear behavior when plotting $\nu^{\star}$ versus $\log(\phi_{\mathcal{B}})$ as a solid line in Fig. 11, which fits to the empirical law

$$\nu^{\star} = D_1 \log \phi_{\mathcal{B}} + D_2, \tag{26}$$

taking D_1 and D_2 as fitting parameters. The slopes for the periodic and aperiodic structures are within the range $D_1 = 0.116 \pm 0.003$, whereas the extrapolated value for $\phi_{\mathcal{B}} = 1$ is $D_2 = 0.363 \pm 0.002$. Extrapolating this behavior to the percolation threshold indicates that the Poisson's ratio may remain finite there, contrary to Young's modulus. The dashed line in the figure represents the Gibson-Ashby model calculation for the effective Poisson's ratio. This calculation of a constant Poisson's ratio of 0.30 falls short to reflect the experimentally observed reduction in the transverse strain to axial strain ratio.

Our findings has two important implications:

---

[13] Although in Roberts and Garboczi's proposal, bulk Young's modulus is recovered at $\phi_{\mathcal{B}} = 1$, Eq. (25) with $C_2 \neq 1$ this is not the case. Thus, extrapolation of Eq. (25) with computed parameters to $\phi_{\mathcal{B}} > 0.5$ should not be made.
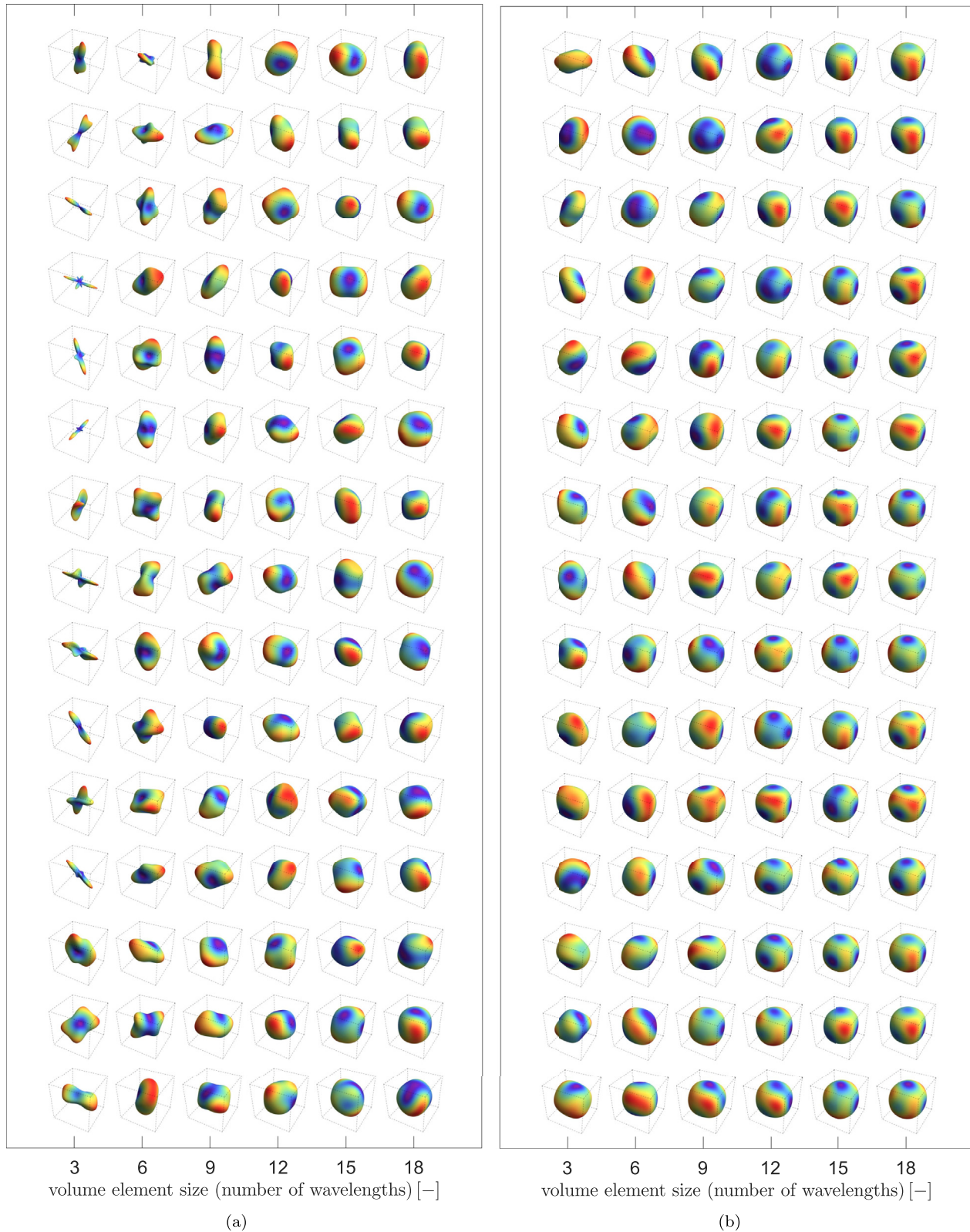
Fig. 9. Directional dependence of normalized Young's modulus for increasing volume element size for (a) 0.20 and (b) 0.50 solid volume fraction. 15 realizations for each volume element size are shown. The results are vertically ordered from less (top) to more (bottom) isotropic. In accordance with Fig. 8, for smaller volume element sizes a high directional dependence of Young's modulus is observed. A highly reduced directional dependence of Young's moduli is observed for 0.50 solid volume fraction as compared to the 0.20 solid volume fraction. The colors correspond to the radius at each surface point with red denoting a maximum and blue denoting a minimum which are individually computed for each figure. Elastic isotropy is represented by a sphere. (For interpretation of the references to colour in this figure legend, the reader is referred to the web version of this article.)
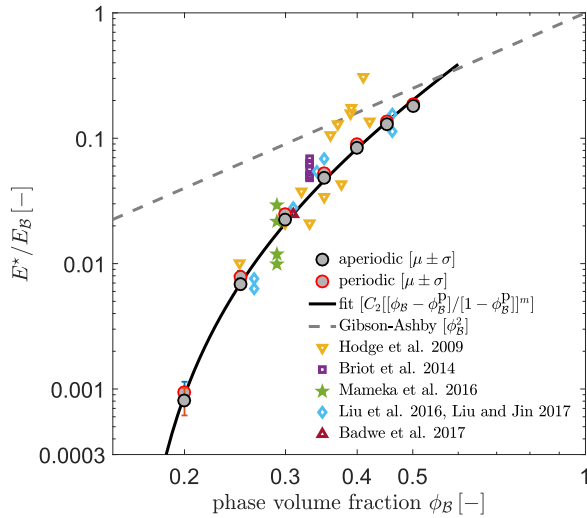
(a)
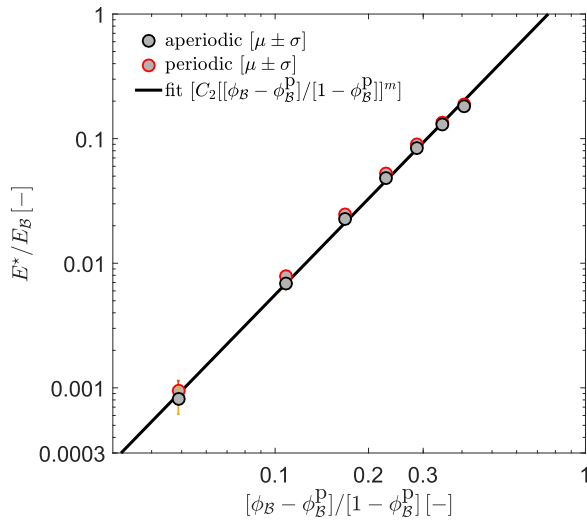
(b)

Fig. 10. Variation of normalized effective Young's modulus, $E^\star/E_\mathcal{B}$, with solid fraction, $\phi_\mathcal{B}$. (a) Log-log representation. Circles: numerical results for aperiodic and periodic structures of present work. Other noncircular symbols: experimental results for nanoporous gold with Refs. [13–15],[17,18,83] Lines: Gibson-Ashby scaling law for open-cell foams, Eq. (24), and modified Roberts-Garboczi law of the present work, Eq. (25), with fitting parameters from part b) of this figure. (b) $E^\star/E_\mathcal{B}$ versus $[\phi_\mathcal{B} - \phi_\mathcal{B}^\mathrm{p}]/[1 - \phi_\mathcal{B}^\mathrm{p}]$ where $\phi_\mathcal{B}^\mathrm{p}$ is the solid fraction of the percolation-to-cluster transition. Circles: numerical results for aperiodic and periodic structures, as in a). Straight line: fit with Eq. (25). Data is presented as mean value μ (dots) and standard deviation σ from analysis of 15 random realizations.

- Firstly, the agreement suggests that the random-field microstructure of our study is in fact a rather accurate representation of the microstructure in experimental nanoporous gold. This provides strong support for the use of similar structures in atomistic simulation studies of nanoporous gold, such as references [19,55,56].
- Secondly, our findings suggest that reducing the solid fraction of nanoporous gold systematically brings its microstructure closer to the percolation-to-cluster transition by reducing its topological genus. That notion is anticipated in Ref. [13] based on findings for the microstructural evolution during coarsening of
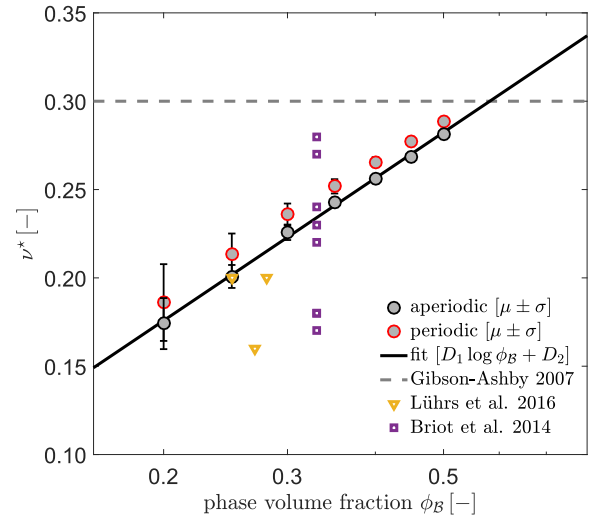

Fig. 11. Variation of effective Poisson's ratio, $\nu^\star$ (linear scale), with solid fraction, $\phi_\mathcal{B}$ (logarithmic scale). Circles: numerical results for aperiodic and periodic structures of present work. Other noncircular symbols: experimental results for nanoporous gold from Refs. [15,16], as detailed in legend. Lines: Gibson-Ashby value for open-cell foams [6] and fit with Eq. (26). Data is presented as mean value μ (dots) and standard deviation σ from analysis of 15 random realizations.

spinodal-like structures [84,85]. The important role of connectivity for the mechanical behavior of nanoporous gold is also advertized in studies determining measures for the scaled genus of nanoporous gold experimentally [23,24]. While such studies remain to be combined with systematic measurement of the mechanical behavior, convincing support comes from a comparative analysis of stiffness and strength, which invokes connectivity to reconcile the observations [14]. By combining information on the topology and on the effective elastic behavior in a wider range of solid fractions, our observations provide the most direct evidence so far for a link between connectivity and stiffness of nanoporous gold. Specifically, we advertise the impact of a systematic drop in connectivity at lesser solid fraction in the material.

The deviation between the stiffness of nanoporous gold and the Gibson-Ashby scaling has led to the proposition of modified scaling laws. Sun et al. [55] proposed a correction that accounts for a transition between bending and tensile deformation as a function of the solid fraction. Huber et al. [47], in their analysis of scaling, also acknowledged that transition but pointed further to the role of structural disorder. Yet, scaling equations that account for the percolation-to-cluster transition have not previously been discussed in context with nanoporous gold. Our results provide strong evidence that this latter phenomenon may hold the key for understanding the systematic deviation between experimental nanoporous gold stiffness data and the classic foam scaling relations.

7. Conclusions

Based on Cahn's method of levelled Gaussian random fields made of random superposed standing waves with constant wavelength, we proposed an efficient and robust method for generating 3D microstructures for nanoporous gold. The method allows a priori fulfillment of the desired solid volume fraction by its inherent Gaussian property. Morphological, topological and elastic

properties of the generated structures were investigated. Comparison of the findings with experimental observations proved that the method accurately produces many morphological and topological features of dealloying-made nanoporous gold. We proposed scaling relations for the variation of the Young's modulus and Poisson's ratio with the solid volume fraction. These relations qualitatively differ from the Gibson-Ashby scaling relations for open-cell foams; the key difference is that systematic changes in the topological genus, which include a percolation-to-cluster transition at a finite solid fraction, are accounted for.

Acknowledgments

Appendix A. Conversion between non-dimensional quantities

Specific surface areas $\mathcal{S}_\mathcal{B}$ and $\mathcal{S}$ as well as genus density G_v are dimensional properties, thus, they depend on the selected length scale. Multiplication with a characteristic size supplies non-dimensionalization and provides quantities which no longer depend on system size or length-scale. Different length scales have been used in the literature, for example Refs. [23,86] used the inverse of the surface area per unit volume, which is defined in Eq. (13); Ref. [24] used the mean ligament diameter instead.

In our computations we have used the length $\tilde{L}$ as the characteristic size. As we have mentioned in Section 4.2, for the symmetric case we can relate the mean ligament diameter with the characteristic size as $L = \tilde{L}/2$. However, in general we expect that the mean ligament diameter is given as $L = h(\phi_\mathcal{B})\tilde{L}$, where $h(\phi_\mathcal{B})$ is a function of the solid volume fraction. Numerically we can find this function by computing the mean ligament diameter of the microstructures for different values of $\phi_\mathcal{B}$ (see Supplementary Material for details). Fig. 12 shows the numerical value of L for different

Fig. 12. Mean ligament diameter as a function of phase volume fraction computed using the methods provided in Refs. [87,88]. Following [88], the ligament diameter (or the local thickness) is defined as the diameter of the largest sphere that fits inside the object and contains the point. Generation of these figures relies on 15 3D random field generations. Two example sections for $\phi_\mathcal{B} = 0.20$ and $\phi_\mathcal{B} = 0.50$ are given for convenience, where the black regions represent solid phase. Data is presented as averages of the means μ (dots) and averages of the standard deviations σ from ligament diameter distribution analysis over 15 random realizations.

values of the volume fraction, where we can fit a simple linear behavior with parameters: $L/\lambda = [0.53\phi_\mathcal{B} + 0.41]$.

Noting that $\lambda = \tilde{L}/\alpha$, we hence arrive at the following empirical relation:

$$L\left(\tilde{L}, \phi_\mathcal{B}\right) = \left[\tilde{L}/\alpha\right][0.53\phi_\mathcal{B} + 0.41], \tag{27}$$

which we can also use to express the inverse of the surface-to-volume ratio as:

$$\mathcal{S}^{-1}\left(\tilde{L}, \phi_\mathcal{B}\right) = \frac{\sqrt{3}}{4\alpha}\tilde{L}e^{\left[\mathrm{erf}^{-1}(2\phi_\mathcal{B}-1)\right]^2}. \tag{28}$$

We can now use these two expressions to convert our computational/analytical findings to the experimentally available results for any value of solid volume fraction.

In their Section 2, Ziehmer et al. [33] report a volume fraction of $\phi_\mathcal{B} = 0.296$ for as-prepared nanoporous gold. In Ref. [24], they determine a scaled connectivity density of $g^Z = 0.124$. This can be converted to the current notation, say $g_v^{Z/S}$, using

$$g_v^{Z/S} = g^Z \times \left[\frac{\tilde{L}}{L}\right]^3. \tag{29}$$

In view of Eq. (27) with $\alpha \simeq 1.23$, for $\phi_\mathcal{B} = 0.296$, one has $L \simeq 0.461\tilde{L}$. Thus, with our scaling, $g_v^{Z/S} \simeq 0.124/0.461^3 = 1.267$. For $\phi_\mathcal{B} = 0.296$, the prediction of the scaled genus density, making use of Eq. (16), is $g_v^S \simeq 1.389$. Thus, we have $g_v^{Z/S}/g_v^S \simeq 0.91$.

In their Table 1, Mangipudi et al. [23] report volume fractions of $\phi_{\mathcal{B},1} = 0.30 \pm 0.1$ and $\phi_{\mathcal{B},2} = 0.32 \pm 0.5$ for their nanoporous gold samples, for which the scaled connectivity densities are $g^{M,1} = 0.067$ and $g^{M,2} = 0.043$, respectively. These can be converted to the current notation, say $g_v^{M,i/S}$ for $i = 1, 2$, using

$$g_v^{M,i/S} = g^{M,i} \times \left[\frac{\tilde{L}}{\mathcal{S}_i^{-1}}\right]^3. \tag{30}$$

In view of Eq. (28) with $\alpha \simeq 1.23$, for $\phi_{\mathcal{B},1} = 0.30$, one has $\tilde{L}/\mathcal{S}_1^{-1} \simeq 2.476$. Thus, with our scaling $g_v^{M,1/S} \simeq 0.067 \times 2.476^3 = 1.017$. For $\phi_\mathcal{B} = 0.30$, the prediction of the scaled genus density, making use of Eq. (16), is $g_v^{S,1} \simeq 1.422$. For $\phi_{\mathcal{B},1} = 0.32$, one has $\tilde{L}/\mathcal{S}_2^{-1} \simeq 2.546$. Thus, with our scaling $g_v^{M,2/S} \simeq 0.043 \times 2.546^3 = 0.710$. The prediction of the scaled genus density, making use of Eq. (16), is $g_v^{S,2} \simeq 1.576$. Thus, we have $g_v^{M,1/S}/g_v^{S,1} \simeq 0.71$ and $g_v^{M,2/S}/g_v^{S,2} \simeq 0.45$.

Appendix B. Supplementary data

Supplementary data related to this article can be found at https://doi.org/10.1016/j.actamat.2018.01.005.

References

[1] J.W. Cahn, Phase separation by spinodal decomposition in isotropic systems, J. Chem. Phys. 42 (1) (1965) 93−99.
[2] M.K. Miller, J.M. Hyde, M.G. Hetherington, A. Cerezo, G.D.W. Smith, C.M. Elliott, Spinodal decomposition in Fe-Cr alloys: experimental study at the atomic level and comparison with computer models-I. Introduction and methodology, Acta Metall. Mater. 43 (9) (1995) 3385−3401.
[3] H. Jinnai, T. Koga, Y. Nishikawa, T. Hashimoto, S.T. Hyde, Curvature determination of spinodal interface in a condensed matter system, Phys. Rev. Lett. 78 (11) (1997) 2248−2251.
[4] C.R. Lopez-Barron, C.W. Macosko, Characterizing interface shape evolution in immiscible polymer blends via 3d image analysis, Langmuir 25 (16) (2009)
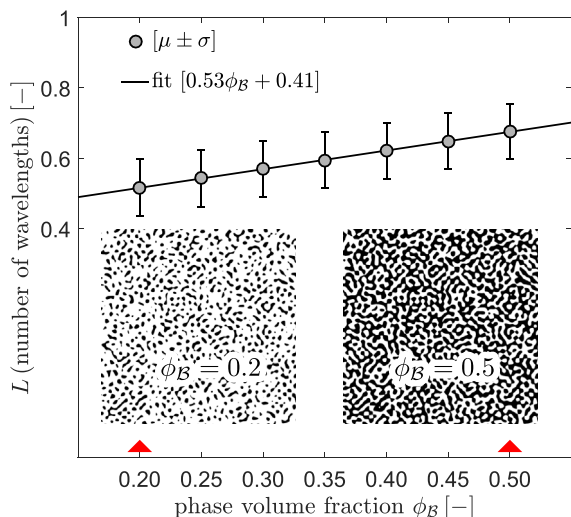
9392—9404.

[5] W. Jahn, R. Strey, Microstructure of microemulsions by freeze fracture electron microscopy, J. Phys. Chem. 92 (8) (1988) 2294—2301.

[6] L.J. Gibson, M.F. Ashby, Cellular Solids: Structure and Properties. Cambridge Solid State Science Series, 2 ed., Cambridge University Press, 1997.

[7] J. Erlebacher, M.J. Aziz, A. Karma, N. Dimitrov, K. Sieradzki, Evolution of nanoporosity in dealloying, Nature 410 (6827) (2001) 450—453.

[8] J. Weissmüller, R.C. Newman, H.-J. Jin, A.M. Hodge, J.W. Kysar, Nanoporous Metals by Alloy Corrosion: Formation and Mechanical Properties, vol. 34, ETATS-UNIS: Materials Research Society, Warrendale, PA, 2009.

[9] R. Li, K. Sieradzki, Ductile-brittle transition in random porous Au, Phys. Rev. Lett. 68 (8) (1992) 1168—1171.

[10] J. Biener, A.M. Hodge, A.V. Hamza, L.M. Hsiung, J. H.Satcher Jr., Nanoporous Au: a high yield strength material, J. Appl. Phys. 97 (2) (2005) 024301.

[11] C.A. Volkert, E.T. Lilleodden, D. Kramer, J. Weissmüller, Approaching the theoretical strength in nanoporous Au, Appl. Phys. Lett. 89 (6) (2006) 061920.

[12] H.-J. Jin, L. Kurmanaeva, J. Schmauch, H. Rösner, Y. Ivanisenko, J. Weissmüller, Deforming nanoporous metal: role of lattice coherency, Acta Mater. 57 (9) (2009) 2665—2672.

[13] N. Mameka, K. Wang, J. Markmann, E.T. Lilleodden, J. Weissmüller, Nanoporous gold-testing macro-scale samples to probe small-scale mechanical behavior, Mater. Res. Lett. 4 (1) (2016) 27—36.

[14] L.-Z. Liu, X.-L. Ye, H.-J. Jin, Interpreting anomalous low-strength and low-stiffness of nanoporous gold: quantification of network connectivity, Acta Mater. 118 (2016) 77—87.

[15] N.J. Briot, T. Kennerknecht, C. Eberl, T.J. Balk, Mechanical properties of bulk single crystalline nanoporous gold investigated by millimetre-scale tension and compression testing, Phil. Mag. 94 (8) (2014) 847—866.

[16] L. Lührs, C. Soyarslan, J. Markmann, S. Bargmann, J. Weissmüller, Elastic and plastic Poisson's ratios of nanoporous gold, Scripta Mater. 110 (2016) 65—69.

[17] N. Badwe, X. Chen, K. Sieradzki, Mechanical properties of nanoporous gold in tension, Acta Mater. 129 (2017) 251—258.

[18] L.-Z. Liu, H.-J. Jin, Scaling equation for the elastic modulus of nanoporous gold with "fixed" network connectivity, Appl. Phys. Lett. 110 (21) (2017) 211902.

[19] B.-N.D. Ngô, A. Stukowski, N. Mameka, J. Markmann, K. Albe, J. Weissmüller, Anomalous compliance and early yielding of nanoporous gold, Acta Mater. 93 (0) (2015) 144—155.

[20] B. Elsner, S. Müller, S. Bargmann, J. Weissmüller, Surface excess elasticity of gold: Ab initio coefficients and impact on the effective elastic response of nanowires, Acta Mater. 124 (2017) 468—477.

[21] C. Soyarslan, E. Husser, S. Bargmann, Effect of surface elasticity on the elastic response of nanoporous gold, J. Nanomech. Micromech. 7 (4) (2017), 04017013−1 −11.

[22] B.-N.D. Ngô, B. Roschning, K. Albe, J. Weissmüller, J. Markmann, On the origin of the anomalous compliance of dealloying-derived nanoporous gold, Scripta Mater. 130 (2017) 74—77.

[23] K.R. Mangipudi, E. Epler, C.A. Volkert, Topology-dependent scaling laws for the stiffness and strength of nanoporous gold, Acta Mater. 119 (2016) 115—122.

[24] K. Hu, M. Ziehmer, K. Wang, E.T. Lilleodden, Nanoporous gold: 3D structural analyses of representative volumes and their implications on scaling relations of mechanical behaviour, Phil. Mag. 96 (no. 32—34) (2016) 3322—3335.

[25] A.P. Roberts, E.J. Garboczi, Computation of the linear elastic properties of random porous materials with a wide variety of microstructure, Proc. Roy. Soc. Lond.: Math. Phys. Eng. Sci. 458 (2021) (2002) 1033—1054.

[26] H. Rösner, S. Parida, D. Kramer, C.A. Volkert, J. Weissmüller, Reconstructing a nanoporous metal in three dimensions: an electron tomography study of dealloyed gold leaf, Adv. Eng. Mater. 9 (7) (2007) 535—541.

[27] T. Fujita, L.-H. Qian, K. Inoke, J. Erlebacher, M.-W. Chen, Three-dimensional morphology of nanoporous gold, Appl. Phys. Lett. 92 (25) (2008) 251902.

[28] T. Krekeler, A.V. Straßer, M. Graf, K. Wang, C. Hartig, M. Ritter, J. Weissmüller, Silver-rich clusters in nanoporous gold, Mater. Res. Lett. 0 (0) (2017) 1—8.

[29] C. Mahr, P. Kundu, A. Lackmann, D. Zanaga, K. Thiel, M. Schowalter, M. Schwan, S. Bals, A. Wittstock, A. Rosenauer, Quantitative determination of residual silver distribution in nanoporous gold and its influence on structure and catalytic performance, J. Catal. 352 (Supplement C) (2017) 52—58.

[30] Y.-C.K. Chen, Y.S. Chu, J. Yi, I. McNulty, Q. Shen, P.W. Voorhees, D.C. Dunand, Morphological and topological analysis of coarsened nanoporous gold by X-ray nanotomography, Appl. Phys. Lett. 96 (4) (2010) 043122.

[31] Y.-C.K. Chen-Wiegart, Y. Wang, S. Chu, W. Liu, I. McNulty, P.W. Voorhees, D.C. Dunand, Structural evolution of nanoporous gold during thermal coarsening, Acta Mater. 60 (12) (2012) 4972—4981.

[32] H.-H. Cho, Y.-C.K. Chen-Wiegart, D.C. Dunand, Finite element analysis of mechanical stability of coarsened nanoporous gold, Scripta Mater. 115 (Supplement C) (2016) 96—99.

[33] M. Ziehmer, K. Hu, K. Wang, E.T. Lilleodden, A principle curvatures analysis of the isothermal evolution of nanoporous gold: quantifying the characteristic length-scales, Acta Mater. 120 (2016) 24—31.

[34] K.R. Mangipudi, V. Radisch, L. Holzer, C.A. Volkert, A FIB-nanotomography method for accurate 3D reconstruction of open nanoporous structures, Ultramicroscopy 163 (2016) 38—47.

[35] A. El-Zoka, B. Langelier, G. Botton, R. Newman, Enhanced analysis of nanoporous gold by atom probe tomography, Mater. Char. 128 (Supplement C) (2017) 269—277.

[36] W. Thomson, On the division of space with minimum partitional area, Acta Math. 11 (1887) 121—134.

[37] D. Weaire, R. Phelan, A counter-example to kelvin's conjecture on minimal surfaces, Phil. Mag. Lett. 69 (2) (1994) 107—110.

[38] L.J. Gibson, M.F. Ashby, The mechanics of three-dimensional cellular materials, Proc. Roy. Soc. Lond.: Math. Phys. Eng. Sci. 382 (1782) (1982) 43—59.

[39] G. Pia, F. Delogu, On the elastic deformation behavior of nanoporous metal foams, Scripta Mater. 69 (11—12) (2013) 781—784.

[40] R. Liu, A. Antoniou, A relationship between the geometrical structure of a nanoporous metal foam and its modulus, Acta Mater. 61 (7) (2013) 2390—2402.

[41] H.A. Schwarz, Gesammelte Mathematische Abhandlungen, Springer, Berlin, 1933.

[42] A.H. Schoen, Infinite Periodic Minimal Surfaces without Self-intersections (NASA Technical Note TN D-5541 (1970)), 1970.

[43] E. Husser, C. Soyarslan, S. Bargmann, Size affected dislocation activity in crystals: advanced surface and grain boundary conditions, Extrem. Mech. Lett. 13 (2017) 36—41.

[44] S. Saane, K. Mangipudi, K. Loos, J.D. Hosson, P. Onck, Multiscale modeling of charge-induced deformation of nanoporous gold structures, J. Mech. Phys. Solid. 66 (Supplement C) (2014) 1—15.

[45] G. Pia, M. Brun, F. Aymerich, F. Delogu, Gyroidal structures as approximants to nanoporous metal foams: clues from mechanical properties, J. Mater. Sci. 52 (Jan 2017) 1106—1122.

[46] E. Detsi, E.D. Jong, A. Zinchenko, Z. Vuković, I. Vuković, S. Punzhin, K. Loos, G. ten Brinke, H.D. Raedt, P. Onck, J.D. Hosson, On the specific surface area of nanoporous materials, Acta Mater. 59 (20) (2011) 7488—7497.

[47] N. Huber, R.N. Viswanath, N. Mameka, J. Markmann, J. Weissmüller, Scaling laws of nanoporous metals under uniaxial compression, Acta Mater. 67 (2014) 252—265.

[48] J. Stavans, The evolution of cellular structures, Rep. Prog. Phys. 56 (6) (1993) 733.

[49] J.A. Glazier, D. Weaire, The kinetics of cellular patterns, J. Phys. Condens. Matter 4 (8) (1992) 1867.

[50] A. Roberts, E. Garboczi, Elastic moduli of model random three-dimensional closed-cell cellular solids, Acta Mater. 49 (2) (2001) 189—197.

[51] K. Mangipudi, P. Onck, Multiscale modelling of damage and failure in two-dimensional metallic foams, J. Mech. Phys. Solid. 59 (7) (2011) 1437—1461.

[52] C. Beckmann, J, Assessment of material uncertainties in solid foams based on local homogenization procedures, Int. J. Solid Struct. 49 (19—20) (2012) 2807—2822. Proceedings of International Union of Theoretical and Applied Mechanics Symposium Mechanics of Liquid and Solid Foams.

[53] C. Redenbach, I. Shklyar, H. Andr, Laguerre tessellations for elastic stiffness simulations of closed foams with strongly varying cell sizes, Int. J. Eng. Sci. 50 (1) (2012) 70—78.

[54] D. Farkas, D.A. Crowson, S.G. Corcoran, Geometric relaxation of nanoporous metals: the role of surface relaxation, Scripta Mater. 56 (11) (2007) 919—922.

[55] X.-Y. Sun, G.-K. Xu, X. Li, X.-Q. Feng, H. Gao, Mechanical properties and scaling laws of nanoporous gold, J. Appl. Phys. 113 (2) (2013) 023505.

[56] D. Farkas, A. Caro, E. Bringa, D. Crowson, Mechanical response of nanoporous gold, Acta Mater. 61 (9) (2013) 3249—3256.

[57] E. Griffiths, S. Bargmann, B. Reddy, Elastic behaviour at the nanoscale of innovative composites of nanoporous gold and polymer, Extreme Mech. Lett. 17 (Supplement C) (2017) 16—23.

[58] R.J. Gaylord, K. Nishidate, Modeling Nature: Cellular Automata Simulations with Mathematica, Springer-Verlag, New York, 1996.

[59] Y. Oono, S. Puri, Study of phase-separation dynamics by use of cell dynamical systems. I. Modeling, Phys. Rev. A 38 (Jul 1988) 434—453.

[60] S. Puri, Y. Oono, Study of phase-separation dynamics by use of cell dynamical systems. II. Two-dimensional demonstrations, Phys. Rev. A 38 (Aug 1988) 1542—1565.

[61] S. Torquato, Random Heterogeneous Materials: Microstructure and Macroscopic Properties, Springer New York, New York, NY, 2002.

[62] J.M. Albina, C. Elsasser, J. Weissmüller, P. Gumbsch, Y. Umeno, Ab initio investigation of surface stress response to charging of transition and noble metals, Phys. Rev. B 85 (12) (2012) 125118.

[63] N.F. Berk, Scattering properties of the leveled-wave model of random morphologies, Phys. Rev. A 44 (Oct 1991) 5069—5079.

[64] M. Teubner, Level surfaces of Gaussian random fields and microemulsions, EPL (Europhys. Lett) 14 (5) (1991) 403.

[65] C. Miehe, A. Koch, Computational micro-to-macro transitions of discretized microstructures undergoing small strains, Arch. Appl. Mech. 72 (4) (2002) 300—317.

[66] A. McBride, J. Mergheim, A. Javili, P. Steinmann, S. Bargmann, Micro-to-macro transitions for heterogeneous material layers accounting for in-plane stretch, J. Mech. Phys. Solid. 60 (6) (2012) 1221—1239.

[67] D. Jeulin, M. O.-S. (Eds.), Mechanics of Random and Multiscale Microstructures, 1 ed, International Centre for Mechanical Sciences 430, Springer-Verlag Wien, 2001.

[68] L. Auvray, J.P. Cotton, R. Ober, C. Taupin, Evidence for zero mean curvature microemulsions, J. Phys. Chem. 88 (20) (1984) 4586—4589.

[69] K. Mangipudi, E. Epler, C. Volkert, Morphological similarity and structure-dependent scaling laws of nanoporous gold from different synthesis methods, Acta Mater. 140 (2017) 337—343.

[70] D. Faurie, P. Djemia, E.L. Bourhis, P.-O. Renault, Y. Roussigné, S. Chérif, R. Brenner, O. Castelnau, G. Patriarche, P. Goudeau, Elastic anisotropy of

polycrystalline Au films: modeling and respective contributions of x-ray diffraction, nanoindentation and brillouin light scattering, Acta Mater. 58 (15) (2010) 4998—5008.

[71] C. Zener, Elasticity and Anelasticity of Metals, University of Chicago, Chicago, 1948.

[72] S.I. Ranganathan, M. Ostoja-Starzewski, Universal elastic anisotropy index, Phys. Rev. Lett. 101 (Aug 2008) 055504.

[73] R. Hill, The elastic behaviour of a crystalline aggregate, Proc. Phys. Soc. 65 (5) (1952) 349.

[74] R. Hill, Elastic properties of reinforced solids: some theoretical principles, J. Mech. Phys. Solid. 11 (5) (1963) 357—372.

[75] K. Terada, M. Hori, T. Kyoya, N. Kikuchi, Simulation of the multi-scale convergence in computational homogenization approaches, Int. J. Solid Struct. 37 (16) (2000) 2285—2311.

[76] S. Hollister, J. Brennan, N. Kikuchi, A homogenization sampling procedure for calculating trabecular bone effective stiffness and tissue level stress, J. Biomech. 27 (4) (1994) 433—444.

[77] K. Sab, B. Nedjar, Periodization of random media and representative volume element size for linear composites, Compt. Rendus Mec. 333 (2) (2005) 187—195.

[78] R. Glüge, M. Weber, A. Bertram, Comparison of spherical and cubical statistical volume elements with respect to convergence, anisotropy, and localization behavior, Comput. Mater. Sci. 63 (2012) 91—104.

[79] E. Garboczi, A. Day, An algorithm for computing the effective linear elastic properties of heterogeneous materials: three-dimensional results for composites with equal phase Poisson ratios, J. Mech. Phys. Solid. 43 (9) (1995) 1349—1362.

[80] K. Schneider, B. Klusemann, S. Bargmann, Fully periodic RVEs for technological relevant composites: not worth the effort!, J. Mech. Mater. Struct. 12 (2017) 471—484.

[81] P. Young, T. Beresford-West, S. Coward, B. Notarberardino, B. Walker, A. Abdul-Aziz, An efficient approach to converting three-dimensional image data into highly accurate computational models, Phil. Trans. Roy. Soc. Lond.: Math. Phys. Eng. Sci. 366 (1878) (2008) 3155—3173.

[82] J. Davis (Ed.), Metals Handbook, ASM International, 1998.

[83] A. Hodge, R. Doucette, M. Biener, J. Biener, O. Cervantes, A. Hamza, Ag effects on the elastic modulus values of nanoporous Au foams, J. Mater. Res. 24 (04) (2009) 1600—1606.

[84] J. Läuger, R. Lay, W. Gronski, The percolation-to-cluster transition during spinodal decomposition of an off-critical polymer mixture. observation by light scattering and optical microscopy, J. Chem. Phys. 101 (8) (1994) 7181—7184.

[85] Y. Kwon, K. Thornton, P.W. Voorhees, Morphology and topology in coarsening of domains via non-conserved and conserved dynamics, Phil. Mag. 90 (1—4) (2010) 317—335.

[86] R. Mendoza, K. Thornton, I. Savin, P. Voorhees, The evolution of interfacial topology during coarsening, Acta Mater. 54 (3) (2006) 743—750.

[87] R. Dougherty, K.-H. Kunzelmann, Computing local thickness of 3D structures with ImageJ, Microsc. Microanal. 13 (S02) (2007) 1678—1679.

[88] T. Hildebrand, P. Rüegsegger, A new method for the model-independent assessment of thickness in three-dimensional images, J. Microsc. 185 (1) (1997) 67—75.